A population of central complex neurons promoting airflow-guided orientation in *Drosophila*

Timothy A. Currier[12], Andrew M. M. Matheson[1], and Katherine I. Nagel[12*]

1 Neuroscience Institute, New York University Langone Medical Center, 435 E 30th St., New York, NY 10016
2 Center for Neural Science, New York University, 4 Washington Pl., New York, NY 10012
*Lead Contact

Abstract

How brain circuits convert sensory signals from diverse modalities into goal-oriented movements is a central question in neuroscience. In insects, a brain region known as the Central Complex (Cx) is believed to support navigation, but how this area organizes and processes diverse sensory cues is not clear. We recorded from genetically-identified Cx cell types in *Drosophila* and presented directional visual, olfactory, and airflow cues known to elicit orienting behavior. We found that a group of columnar neurons targeting the ventral fan-shaped body (ventral P-FNs) were consistently tuned for airflow direction. Silencing these neurons prevented flies from adopting stable orientations relative to airflow in closed-loop flight. Specifically, silenced flies selected improper corrective turns following changes in airflow direction, but not following airflow offset, suggesting a specific deficit in sensory-motor conversion. Our work provides insight into the organization and function of the insect navigation center.

keywords: navigation, orientation, insect, central complex, *Drosophila*, electrophysiology, airflow, mechanosensory, multi-sensory

Introduction

Foraging for food, locating mates, and avoiding predation all depend on an animal's ability to navigate through complex multi-sensory environments. Many animals, including rodents (Gire et al., 2016), birds (Holland et al., 2009), fish (Bianco and Engert 2015), insects (Dacke et al., 2019; Cardé and Willis, 2008) and nematodes (Lockery, 2011), are known to compare and combine visual, mechanosensory and olfactory cues to achieve their navigational goals. Identifying the brain regions and circuit organizations that support navigation with respect to different modalities is a fundamental question in neuroscience.

Although it has received less attention than vision or olfaction, flow of the air or water is a critical mechanosensory cue for animals navigating in aquatic (Montgomery et al., 1997), terrestrial (Yu et al., 2016a), and air-borne (Alerstam et al., 2011; Reynolds et al., 2010) environments. While the primary sensors that detect flow are well-described in fish (Suli et al., 2007), rodents (Yu et al., 2016b), and insects (Budick et al., 2007; Yorozu et al., 2009, Suver et al. 2019), the higher brain circuits that use flow signals to guide navigation remain unknown. In particular, it is unknown whether distinct central populations process flow cues to guide orientation, or whether such cues are handled by the same circuits that support orientation driven by different sensory modalities.

In insects, a conserved brain region known as the Central Complex (Cx) is thought to control many aspects of navigation behavior (Strauss and Heisenberg, 1993). The Cx is a highly organized neuropil consisting of four primary subregions: the Protocerebral Bridge (PB), the Ellipsoid Body (EB), the Fan-shaped Body (FB), and the paired Noduli (NO). Columnar neurons recurrently connect these regions to each other, while tangential neurons targeting different layers of the EB and FB provide a large number of inputs from, and a smaller number of outputs to, the rest of the brain (Hanesch et al., 1989; Wolff et al., 2015, Franconville et al., 2018).

Because Cx cell types are numerous and diverse, it is not yet clear whether they are primarily multi-sensory, or whether different Cx compartments preferentially represent different modalities. Many Cx neurons have been shown to respond to visual stimuli, such as polarized light or optic flow (Heinze and Homberg, 2007; Weir and Dickinson, 2015; Stone et al., 2017), and to mechanical activation of the antennae or halteres (Ritzmann et al., 2008; Phillips-Portillo, 2012; Kathman and Fox, 2019). Many neurons within the Cx also exhibit activity correlated with motor behavior, such as turning (Green et al., 2017; Turner-Evans et al., 2017; Shiozaki et al., 2020) and forward velocity (Martin et al., 2015). In the EB, a group of columnar neurons known as "compass neurons" (or E-PGs) exhibit an abstract representation of heading that is derived from both visual and self-motion cues (Seelig and

72 Jayaraman, 2013; Green et al., 2017; Fisher et al., 2019), while a group known as P-ENs participate in
73 rotating this heading representation (Green et al., 2017; Turner-Evans et al., 2017). The development
74 of *Drosophila* genetic lines that target specific Cx neuron types (Wolff et al. 2015; Wolff and Rubin,
75 2018) provides a means to systematically address how sensory and motor signals are organized in the
76 Cx.
77
78 Another open question about Cx organization is the precise role that its structures play in guiding
79 navigation and orientation behavior. Genetic malformations of the EB and FB in *Drosophila* broadly
80 disrupt sensory-guided locomotion (Strauss and Heisenberg, 1993), while other data are consistent
81 with a role for the Cx in selecting from possible movements during ongoing navigation. For example,
82 electrolytic lesions of the FB in cockroaches alter their climbing and turning maneuvers (Harley and
83 Ritzmann, 2010). Additionally, silencing compass neurons disrupts menotaxis — straight-line
84 navigation by keeping a visual landmark at an arbitrary orientation — but not the ability to fixate a
85 visual landmark per se (Giraldo et al., 2018; Green et al., 2019). Thus, the relationship between the
86 sensorimotor representations and functional roles of particular Cx populations is an active area of
87 investigation.
88
89 Here we investigated the representation of different sensory modalities in diverse Cx columnar cell
90 types. We focused on three stimuli known to elicit orientation behavior in *Drosophila*: a vertical visual
91 stripe, directional airflow, and an attractive odor. Flies fixate vertical stripes while walking and in flight
92 (Reichardt and Poggio, 1976; Heisenberg and Wolf, 1979; Maimon et al. 2008) and tend to orient away
93 from an airflow source (Currier and Nagel 2018). The addition of an attractive odorant to airflow
94 switches orientation from downwind to upwind (van Bruegel et al. 2014, Alvarez-Salvado 2018). We
95 used split-GAL4 lines to target 8 columnar neuron types that target different layers of the FB and EB,
96 and made whole cell recordings of individual neurons responding to stimuli of multiple modalities and
97 directions.
98
99 We found that, while many columnar neurons exhibited responses to multiple stimuli, two groups of
100 neurons targeting the ventral FB and 3rd NO compartment were robustly tuned for the direction of
101 airflow. Based on their anatomy, we call these neurons “ventral P-FNs.” Recordings from different
102 columns suggest that the tuning of ventral P-FNs primarily reflects the hemisphere in which their cell
103 body is located. Left hemisphere ventral P-FNs were excited by airflow from the left and inhibited by
104 airflow from the right, and vice-versa. Genetic silencing experiments suggest that these neurons
105 support normal orientation to airflow in a closed-loop flight simulator. In particular, ventral P-FNs are
106 required to convert changes in airflow direction into heading-appropriate turning responses. In
107 contrast, turn rate distributions and directional responses to a drop in air speed were preserved in

silenced flies, suggesting that sensory and motor functions remain intact. These results argue that ventral P-FNs play a specific role in linking a directional sensory input to corrective motor action. Collectively, our data expand our understanding of sensory processing and integration in the Cx, and suggest that it may contain distinct populations that process cues of different modalities to achieve navigational goals.

Results

Airflow dominates responses to directional sensory cues in a set of Cx columnar neurons.

To assess the potential organization of directional sensory cues in the Cx, we used whole-cell electrophysiology to perform a survey of cell types that target the protocerebral bridge. We selected this group because they are largely intrinsic to the Cx, innervate different layers of the FB and EB, and can be targeted using publicly available split-GAL4 driver lines (Wolff and Rubin, 2018). We expressed GFP in each population and made whole-cell recordings while we presented flies with the following sensory cues, either alone or in combination: a high contrast vertical bar, airflow generated by a pair of tubes, and apple cider vinegar, which could be injected into the airstream (Fig. 1A & 1B, right). These cues were chosen because they have each been previously shown to induce reliable orienting behavior (Currier and Nagel, 2018; Alvarez-Salvado et al., 2018). Each stimulus combination was presented from four directions: frontal, rear, ipsilateral, and contralateral (Fig. 1B, left). We monitored fly activity with an infrared camera and discarded the few trials that contained flight behavior.

We first noticed that Cx columnar cell types possessed diverse baseline activity. Some cell types, such as P-EN2 and P-F_2N_3, showed rhythmic fluctuations in membrane potential, evident in the timecourses and distributions of membrane potential (Fig. 1C and S1). Rhythmic neurons exhibited broader membrane potential distributions than less rhythmic neurons (Fig. 1C, right and Fig. S1B&C). P-F_3LC, for example, showed stable baseline activity and a lower characteristic resting potential. We did not observe any correlation between fly behavior and the presence or absence of oscillations, but resting membrane potential did rarely fluctuate with leg movements. Input resistance varied by cell type, with values ranging from 1.5 - 10 GOhm (Fig. S1D).

We next turned our attention to the sensory responses of Cx columnar cell types. We found that, although most neurons responded to each cue in some manner, airflow responses were generally larger than stripe responses across cell types in the survey. In P-F_1N_3 neurons, for example, large directionally tuned spiking responses were observed during airflow presentation, but not stripe

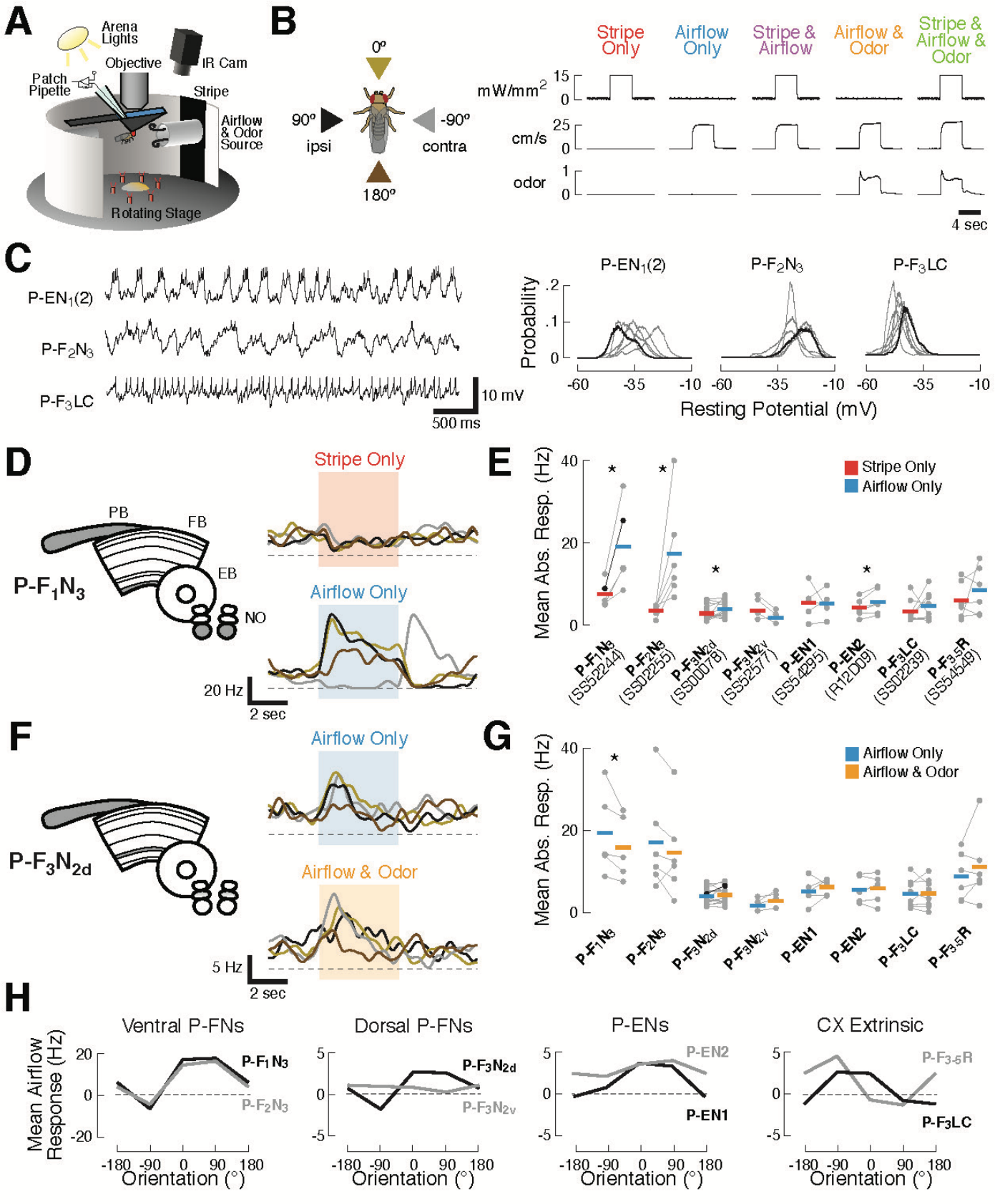
A
Arena Lights
Objective
IR Cam
Patch Pipette
Stripe
Airflow & Odor Source
Rotating Stage
B
0°
90° ipsi
-90° contra
180°
Stripe Only
Airflow Only
Stripe & Airflow
Airflow & Odor
Stripe & Airflow & Odor
mW/mm2
cm/s
odor
4 sec
C
P-EN1(2)
P-F2N3
P-F3LC
10 mV
500 ms
Probability
Resting Potential (mV)
D
PB
FB
EB
NO
P-F1N3
Stripe Only
Airflow Only
20 Hz
2 sec
E
Mean Abs. Resp. (Hz)
Stripe Only
Airflow Only
P-F1N3 (SS52244)
P-F2N3 (SS02255)
P-F3N2d (SS00078)
P-F3N2v (SS52577)
P-EN1 (SS54295)
P-EN2 (R12D09)
P-F3LC (SS02239)
P-F3-5R (SS54549)
F
P-F3N2d
Airflow Only
Airflow & Odor
5 Hz
2 sec
G
Mean Abs. Resp. (Hz)
Airflow Only
Airflow & Odor
P-F1N3
P-F2N3
P-F3N2d
P-F3N2v
P-EN1
P-EN2
P-F3LC
P-F3-5R
H
Mean Airflow Response (Hz)
Ventral P-FNs
P-F1N3
P-F2N3
Dorsal P-FNs
P-F3N2d
P-F3N2v
P-ENs
P-EN2
P-EN1
CX Extrinsic
P-F3-5R
P-F3LC
Orientation (°)

Figure 1. Sensory responses and preferred airflow direction vary across Cx columnar cell types.

(A) Experimental preparation. We targeted single neurons for patching using cell type-specific expression of GFP. Flies were placed in an arena equipped with rotatable stimulus delivery and live imaging of behavior. All data shown are from awake non-flying animals.
(B) Stimulus details. Left: cue presentation directions. Front (0°, gold), rear (180°, brown), ipsilateral (90°, black), and contralateral (-90°, grey) to the recorded neuron. Right: stimulus validation. Each plot shows measurements from a photodiode (top), anemometer (middle), and photo-ionization detector (PID, bottom). PID units are arbitrary. The five stimulus combinations were: a high contrast stripe illuminated by 15 mW/cm2 ambient lighting (red), a 25 cm/s airflow stream (blue), stripe and airflow together (purple), airflow and 20% apple cider vinegar together (orange), and all three modalities simultaneously (green). Each trace is 12 sec long. Simultaneous cues were presented from the same direction.
(C) Rhythmic and tonic baseline activity in a subset of Cx columnar neuron types. Left: raw membrane potential over time for three example neurons. P-EN2 and P-F_1N_3 show rhythmic activity at different frequencies, while P-F_1LC fires tonically at rest. Right: resting membrane potential probability distributions for each recorded neuron of the types shown (gray). Example neurons in black. Rhythmic neurons exhibit broad distributions, while tonic neurons show tight distributions. See also Fig. S1.
(D) Left: Cx neuropils innervated by P-F_1N_3 neurons (gray). PB, Protocerebral Bridge; FB, Fan-shaped Body; EB, Ellipsoid Body; NO, noduli. Right: PSTHs for a single P-F_1N_3 neuron. Each trace represents the mean of four presentations of stripe alone (red, top) or airflow alone (blue, bottom) from one direction. Colors representing different directions as illustrated in (B). Colored boxes indicate the 4 sec stimulus period. Dashed line indicates 0 Hz.
(E) Responses to airflow (blue) versus stripe (red) for each neuron type. Gray dots indicate the mean spiking response of each cell (1 sec stimulus minus 1 sec baseline) to four trials from the direction producing the strongest response (see Methods). Colored bars: mean across cells. The example P-F_1N_3 neuron from (D) is shown in black. Significant differences ($p < 0.05$ by rank-sign test) between modalities are marked with an asterisk. For additional detail, see Fig. S2.
(F) Left: Cx neuropils innervated by P-F_2N_3 neurons. Right: PSTHs for a single P-F_2N_3 neuron. Each trace represents the mean of four presentations of airflow alone (blue, top) or airflow and odor together (orange, bottom) from one direction. Plot details as in (D).
(G) Responses to odorized airflow (orange) versus airflow alone (blue) for all cell types recorded. Asterisk: odor significantly reduces the response of P-F_2N_3. Plot details as in (E). For additional detail, see Fig. S2.
(H) Mean airflow response across cells as a function of airflow direction for each cell type. Cell types are plotted in groups of two (gray, black) according to broad anatomical similarities. Note different vertical axis scales. For additional detail, see Fig. S2.

presentation (Fig. 1D). To assess this difference across cell types, we identified the cue direction(s) that elicited the largest stripe and airflow responses for each recorded neuron. We then took the mean absolute value of responses to that direction (relative to baseline), and plotted these values as a function of sensory condition for each cell (Fig. 1E). For every cell type except P-F_3N_{2v} and P-EN1, the cross-fly mean airflow response was larger than the mean stripe response. This difference was significant for half of the cell types surveyed: P-F_1N_3, P-F_2N_3, P-F_3N_{2d}, and P-EN2. Airflow responses for P-F_1N_3 and P-F_2N_3 were particularly large. While response magnitudes no doubt depend on stimulus intensity (airflow velocity and stripe contrast), we know that our cues elicit orienting responses of approximately equal magnitude in a flight simulator (Currier and Nagel, 2018). Therefore, these responses reflect differential neural encoding of stimuli with similar behavioral relevance.

Conversely, adding odor to the airflow stream had only mild effects on Cx columnar neuron responses. While single cells did sometimes show increases or decreases in spiking activity in the odor condition (Fig. 1F), we only observed reliable differences for P-F_1N_3 and P-F_2N_3, where odor slightly suppressed the airflow response (Fig. 1G). Of these cell types, only P-F_1N_3 responses were significantly reduced.

Because of the strong airflow responses we observed, we next examined directional tuning in the airflow condition (Fig. 1H). Most of the surveyed cell types preferred ipsilateral airflow, with two cell types deviating from this trend: P-F_3LC and P-$F_{3\text{-}5}$R. These neurons instead preferred contralateral

airflow. In contrast to this strong directional preference in the airflow condition, tuning strength in the visual condition was relatively weak for all recorded cell types (Fig. S2).

Overall, modality-specific responsiveness and preferred airflow direction appeared to vary with broad anatomical features of Cx columnar cell types. In particular, “ventral P-FNs,” which target layer 3 of the NO and ventral FB layers, had large airflow responses, strong ipsilateral tuning, and olfactory suppression. “Dorsal P-FNs,” which target layer 2 of the NO, and “P-ENs,” which target layer 1 of the NO, both displayed modest sensory responses and ipsilateral airflow tuning in most cases. The last category, “Cx extrinsic” neurons, target neuropil outside the Cx proper and were the only cells in our survey to prefer contralateral airflow. We next examined how each cell type integrated multi-sensory cues.

Multi-sensory integration in Cx columnar neurons is largely linear, with some cell-type specific diversity.

To understand the computational principles that govern cue integration in Cx columnar neurons, we first compared multi-sensory responses to the sum of single modality responses (Fig. 2A). Summation is a simple circuit principle that is naturally achieved by an upstream neuron or neurons passing multimodal cues to a single downstream cell. For each cell type, we found the mean response to the airflow-plus-stripe condition for each cue direction. We then plotted these multi-sensory responses against the sum of the mean airflow response and the mean stripe response from the same directions (Fig. 2A, left). When we plotted these measures for each cell type, we found that most points fell on or near the diagonal, indicating that multi-sensory responses are, on average, approximately equal to the sum of single modality responses. This trend of near-perfect summation was also true when all three modalities were presented simultaneously (Fig. 2A, right). These results suggest that poly-modal integration in Cx columnar neurons generally proceeds via a summation principle.

Because of the diverse sensory responses observed in our survey, we wondered whether integration principles may also differ across individual members of a single cell type. To answer this question, we evaluated stripe and airflow integration for single cells (Fig. 2B-E). Broadly, we found that integration diversity was small for some cell types, but large for others. P-EN2 neurons, for example, showed remarkably consistent summation. Single neuron spiking responses to multi-sensory cues strongly resembled the responses to single modality cues across all P-EN2s (Fig. 2C, top). To evaluate summation in a scale-free manner, we found the correlation coefficient between the mean response timecourse to the multi-sensory condition and each of the single modality conditions (Fig. 2D). To do

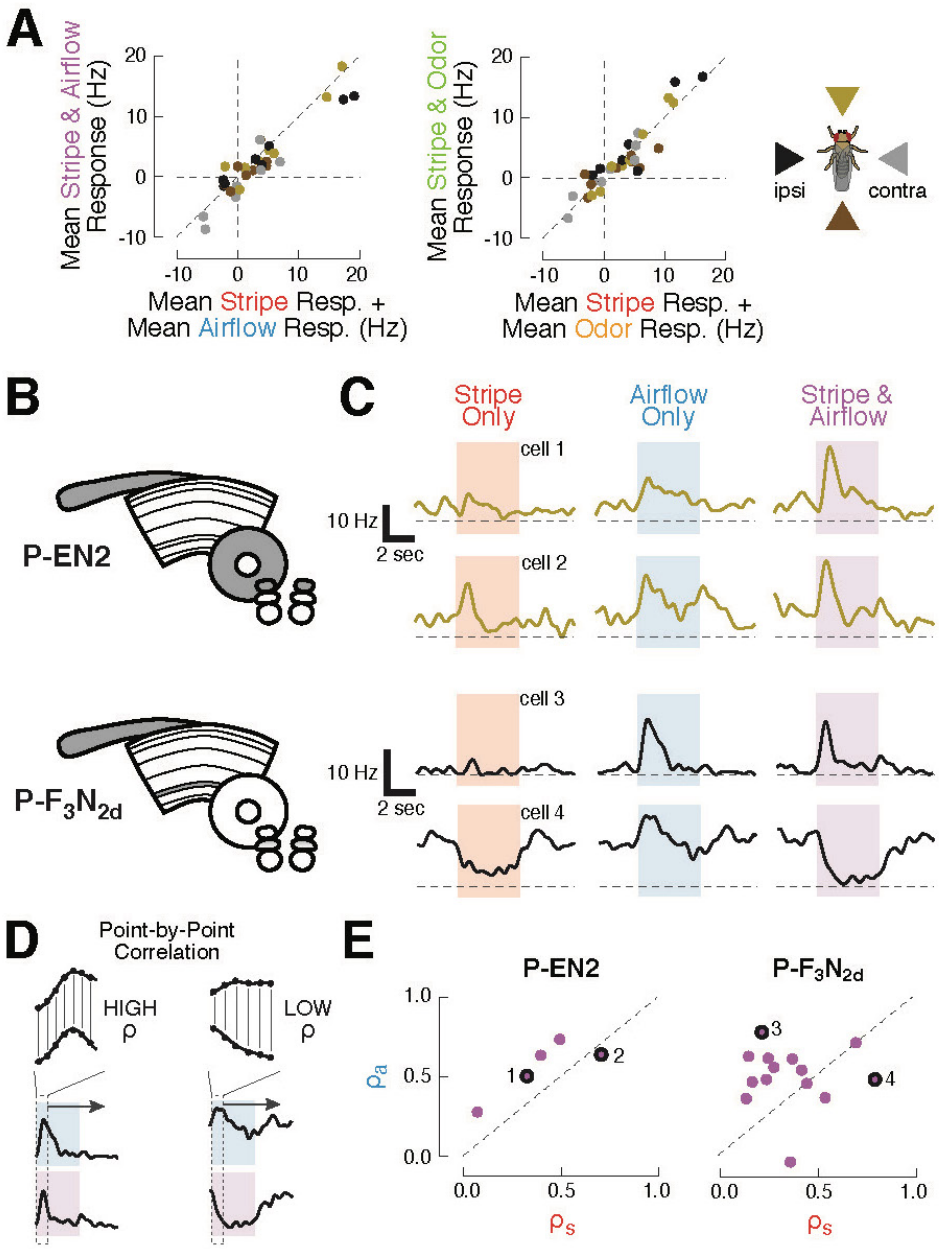

Figure 2. Cx columnar neurons sum inputs from different modalities on average, but show diverse integration strategies at the level of single cells.

(A) Summation of multimodal cues. Left: mean spiking response to stripe & airflow together versus sum of mean stripe alone and airflow alone responses. Each point represents the response of one cell type to cues from one direction. Right: mean spiking response to stripe & airflow & odor versus sum of mean stripe alone response and mean airflow & odor response. Colors indicate cue direction (far right). Data falling along the diagonals indicate perfectly weighted summation.
(B) Cx neuropils innervated by example cell types P-EN2 and PFN$_{2d}$.
(C) PSTHs of two neurons from each cell type. Curves represent mean firing rate across four trials of each stimulus from a single direction. Colored boxes indicate the four second stimulus period. Dashed lines indicate 0 Hz. Top: example P-EN2 neurons responding to frontal cues. In both cases, the multi-sensory response (purple) is a weighted sum of the single modality responses (red, blue). Bottom: PFN$_{2d}$ neurons responding to ipsilateral cues. The multi-sensory response reflects one modality, but not the other.
(D) Correlation method for computing response similarity. We computed a point-by-point correlation between the mean baseline-subtracted firing rate time-courses of multi-sensory responses and responses to a single modality, across all stimulus directions. Similar traces result in high ρ
(E) Similarity (calculated as in D) of the multimodal response (stripe + airflow) to each single modality response. Data along the diagonal indicates that the multi-sensory response is equally similar to the stripe alone and airflow alone responses, a hallmark of summation. Data off diagonal indicates that one modality dominates the multi-sensory response. The four example cells from (C) are labeled with numbers and black rings. P-EN2 neurons consistently sum stripe and airflow responses (top), while PFN$_{2d}$ neurons integrate with greater diversity (bottom).

this, we concatenated each cell's mean spiking responses to stimuli presented from different directions (-90°, 0°, 90°, 180°), with the baseline period removed. We then took the point-by-point correlation between the concatenated multi-sensory response and the single modality responses, which yielded a pair of correlation coefficients (ρ_a for airflow and ρ_s for stripe). A coefficient of 1 indicates that the multi-sensory and single modality data varied over time in perfect synchrony. Conversely, a coefficient closer to 0 indicates that these signals did not vary together. When we plotted these coefficients against one another (Fig. 2E, but also see Fig. S3), we found that the P-EN2 data lie along the diagonal, indicating that the stripe and airflow responses equally resemble the multi-sensory response for each neuron.

211 In contrast, P-F_3N_{2d} neurons show much greater integration diversity. While some cells displayed
212 multi-sensory activity that was dominated by the stripe response, others were dominated by the
213 airflow response (Fig. 2C, bottom). Indeed, the correlation coefficients for P-F_3N_{2d} reveal a full range of
214 modality preferences (Fig. 2E, right). We did not observe any obvious relationship between single
215 neuron anatomy and the method of integration used by that cell. Thus, while summation appears to
216 govern P-F_3N_{2d} integration on average, individual neurons show an array of sensory integration
217 strategies. This trend of summation on average, but diversity at the single cell level, was found for
218 many of the surveyed cell types (Fig. S3).
219
220
221 *Ventral P-FNs are tuned to ipsilateral airflow, with subtle differences across columns.*
222
223 At the conclusion of our survey, ventral P-FNs (P-F_1N_3 and P-F_2N_3) stood out as possessing the most
224 robust sensory responses. We first examined the activity of P-F_2N_3, which had the strongest airflow
225 responses in our survey, in greater detail (Fig. 3A-G). These cells has resting membrane potentials
226 between -30 and -25 mV, and input resistances around 3 GOhm (Fig. S1). P-F_2N_3s showed strong
227 spiking responses to single presentations of ipsilateral airflow, and active inhibition followed by offset
228 spiking during single presentations of contralateral airflow (Fig. 3B&D). Spiking activity in response to
229 ipsilateral and contralateral airflow was relatively consistent from trial to trial, while frontal and rear
230 airflow elicited more diverse responses relative to baseline on each trial (Fig. 3D). On average, P-F_2N_3
231 neurons showed graded membrane potential and spiking responses to airflow, but not to the stripe
232 (Fig. 3C&E).
233
234 To assess how additional sensory modalities modulate this directional airflow tuning, we plotted the
235 spiking response as a function of stimulus orientation for each combination of cues (Fig. 3F). We found
236 that mean tuning across the population did not change when the stripe, odor, or both, were added to
237 airflow. Each P-F_2N_3 neuron showed a large airflow correlation coefficient and a small visual coefficient
238 (Fig. 3G), indicative of multi-sensory responses that strongly resemble the airflow-only response. P-
239 F_1N_3 sensory activity was similar, except for the olfactory suppression noted above (Fig. 3H&I).
240
241 Like many other columnar cell types, individual ventral P-FNs target one Cx column, with cell bodies in
242 each hemisphere collectively innervating all eight columns (Wolff et al., 2015). We next asked whether
243 neurons innervating different columns show distinct directional tuning, as has been previously
244 observed for polarized light cues (Heinze and Homburg, 2007) and visual landmarks (Green et al.,
245 2017; Fisher et al. 2019). To address this question, we recorded from a larger set of P-F_2N_3 neurons
246 while explicitly attempting to sample from a range of Cx columns (Fig. 4A). For this experiment, we

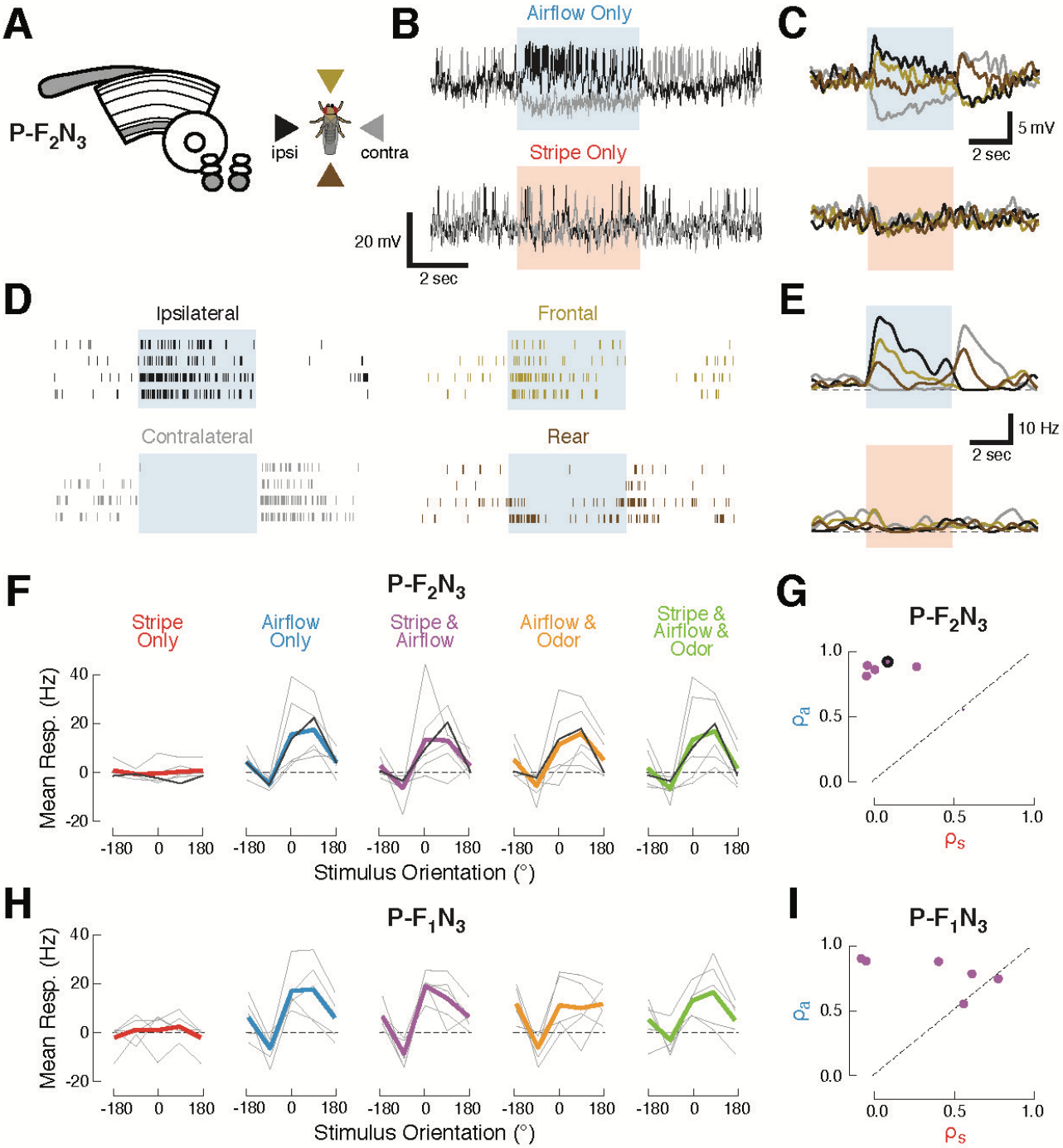

Figure 3. Ventral P-FNs selectively respond to directional airflow.

(A) Left: Cx neuropils innervated by $P\text{-}F_1N_3$. Right: color key for directional stimuli.
(B) Example trials from a single $P\text{-}F_1N_3$ neuron. Raw membrane potential for single presentations of airflow alone (blue, top) or stripe alone (red, bottom) for ipsilateral (black) and contralateral (gray) directions. Colored box indicates 4 sec stimulus period. Baseline V_m = -28 mV.
(C) Average V_m (over 4 trials) for the example neuron shown in (B). Colors represent directions as shown in (A). Stimulus period represented as in (B).
(D) Spike response rasters for the example neuron shown in (B). Colors and stimulus period as in (C).
(E) PSTHs for the example neuron in (B). Colors and stimulus period as in (C).
(F) $P\text{-}F_2N_3$ direction tuning for each cue set showing that responses to airflow are not modulated by other modalities. Mean spiking response minus baseline for each recorded cell as a function of stimulus direction (gray lines). The example neuron in (B-E) is shown in black. Mean tuning across cells shown in thick colored lines.
(G) Similarity (as in Fig. 2C) of $P\text{-}F_2N_3$ multi-sensory (stripe + airflow) responses to airflow alone and and stripe alone. Response to stripe + airflow is highly similar to airflow alone. Example neuron marked in black.
(H) Direction tuning for the second type of ventral P-FN, $P\text{-}F_1N_3$. Note that odor subtly inhibits airflow-evoked responses (as shown in Fig. 1G).
(I) Same as (G), but for $P\text{-}F_1N_3$.

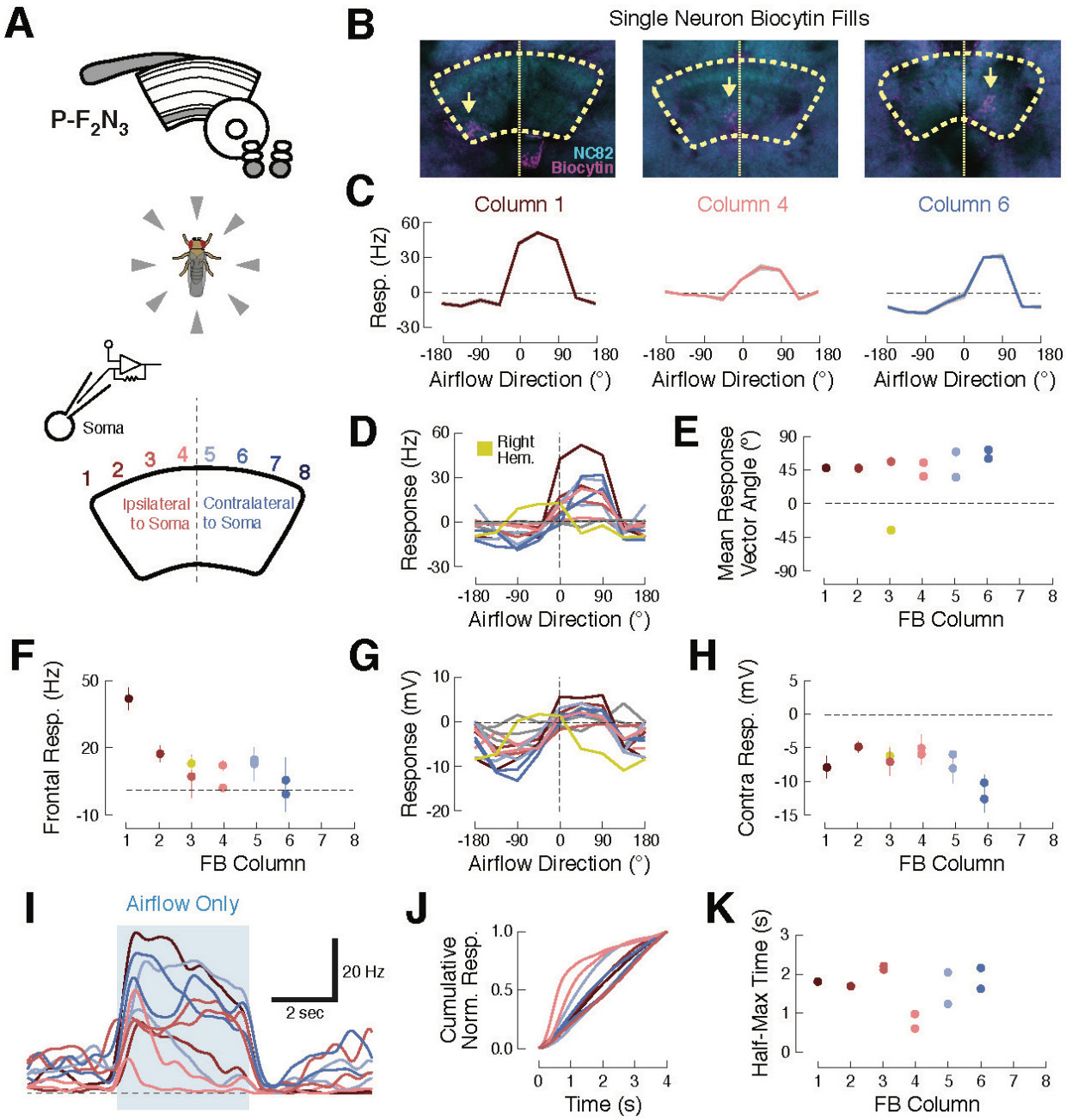

Figure 4. Ventral P-FNs are excited by ipsilateral airflow, but exhibit subtle differences across columns.

(A) Top: Cx neuropils innervated by P-F_2N_3. Bottom: experimental setup. We presented airflow from eight directions and identified the column innervated by each patched neuron by filling the cell with biocytin.
(B) Biocytin fills (magenta) for three example cells innervating columns 1 (left), 4 (middle), and 6 (right). Yellow arrows indicate FB portions of fills. Neuropil in cyan. Thick dashed line indicates the borders of the FB and thin dotted line shows the midline.
(C) P-F_2N_3 airflow tuning is similar across FB columns. Mean +/- SEM spiking response as a function of airflow direction for the three example cells shown in (B). Colors reflect innervated column, as in (A).
(D) Mean spiking response as a function of airflow direction for all recorded P-F_2N_3 neurons. Colors as in (A). A single right hemisphere neuron, as a control, is shown in yellow. Gray curves indicate cells for which no anatomy data could be recovered.
(E) Mean response vector angle as a function of column for each recorded neuron. Colors as in (D).
(F) Mean +/- SEM spiking response to frontal airflow as a function of column. Colors as in (A).
(G) Mean membrane potential response as a function of airflow direction for each neuron. Colors as in (D).
(H) Mean +/- SEM membrane potential response to contralateral airflow as a function of column. Colors as in (D).
(I) Timecourse (PSTH) of airflow responses to ipsilateral airflow for the same P-F_2N_3 neurons (average of 4 trials). Blue box indicates 4 sec stimulus. Colors as in (A).
(J) Cumulative normalized response for each neuron during the 4 sec stimulus, normalized to its mean integrated response. Transient responses show fast rise times and tonic responses show slower rise times. Colors as in (A).
(K) Time to half-max (a measure of response transience) as a function of column. Colors as in (A).

presented airflow from eight directions and omitted other sensory modalities. To identify the FB columns targeted by our recorded neurons, we filled each cell with biocytin and visualized its anatomy after the recording session (Fig. 4B&C).

Across FB columns, we found that left-hemisphere P-F_2N_3 neurons responded most strongly to airflow presented from the left (90º, ipsilateral) and were inhibited by airflow from the right (-90º, contralateral). One right hemisphere neuron, recorded as a control, was excited by airflow from the right (-90º) and inhibited by airflow from the left (90º). Thus, all P-F_2N_3 neurons show a preference for airflow presented ipsilateral to their cell bodies (Fig. 4D&E).

However, we also noticed some subtle differences in tuning that did vary with column. The spiking response to frontal airflow (0°) was strongest in the ipsilateral-most column 1, and was weaker in more contralateral columns (Fig. 4F). To examine the strength of inhibition, we also plotted membrane potential tuning curves (Fig. 4G). Membrane potential responses to contralateral also airflow varied by column, with contralateral columns exhibiting the greatest inhibition relative to baseline (Fig. 4H). Thus, while the population of P-F_2N_3 neurons does not create a “map” of airflow direction, the tuning of individual cells does vary subtly by column.

We also found that P-F_2N_3 neurons showed temporally diverse airflow responses (Fig. 4I). Some neurons showed sustained activity during the stimulus period, while others displayed only transient responses to airflow presentation. To quantify these differences, we first normalized each response to the total integrated firing rate over the 4 sec stimulus period. We then plotted the cumulative normalized response as a function of time since stimulus onset (Fig. 4J). In these plots, transient responses have a steep early slope and tonically responsive cells have lower slopes. We used the time to half-max as a measure of how phasic versus tonic a cell’s response was (Fig. 4K). The most phasic responses were found in P-F_2N_3 neurons that innervated medial FB columns (4 and 5).

These data support two conclusions. First, ventral P-FNs respond primarily to airflow, and not to the other stimuli presented in our cue set. Second, airflow tuning in P-F_2N_3 neurons depends on the location of cell bodies and the column they innervate. Thus, airflow from different directions is represented by different patterns of P-F_2N_3 activation in left- and right-hemisphere neurons innervating the same column.

Ventral P-FNs are required to orient to airflow in tethered flight

285 Because ventral P-FNs show robust airflow responses, we wondered whether these neurons play a
286 role in orientation to airflow. We addressed this question with a previously designed closed-loop flight
287 simulator that uses an infrared camera to monitor the fictive turning of a tethered animal flying in the
288 dark (Fig. 5A). This turn signal drives rotations of an airflow tube, allowing flies to control their
289 orientation with respect to that flow. In previous experiments, we observed that flies prefer to orient
290 away from the source of flow (Currier and Nagel, 2018).
291
292 We first asked whether silencing ventral P-FNs (P-F_1N_3 and P-F_2N_3) impairs normal airflow-based
293 orienting. We compared behavior in flies where these neurons were silenced with Kir2.1 to control flies
294 where Kir2.1 was driven by an *empty-GAL4* cassette. Consistent with our previous results, control flies
295 adopted stable orientations away from the airflow source (Fig. 5C-F). When we calculated the mean
296 orientation vector for each control fly, we found that they all preferred orientations roughly opposite
297 the flow source, near 180° (Fig. 5D). When either type of ventral P-FN was silenced with Kir2.1, flies
298 displayed partially impaired orientation ability (Fig. 5D). These groups showed increased orienting
299 toward the flow (Fig. 5E) and reduced orientation stability (Fig. 5F) compared to controls, although
300 both effects were moderate.
301
302 Given the similar sensory responses of P-F_1N_3 and P-F_2N_3, we reasoned that they might serve
303 overlapping roles. We therefore sought a driver line that labeled both classes of ventral P-FN, and
304 identified *R44B10-GAL4* as one such line with minimal off-target expression (Figs. 5B and S4).
305 Silencing *R44B10-GAL4* neurons with Kir2.1 produced a more severe phenotype (Fig. 5C). Compared
306 to controls, these flies showed less stable orientation to airflow (Fig 5D), spent significantly more time
307 oriented toward the airflow source (Fig. 5E), and had reduced fixation strength (Fig. 5F). Collectively,
308 these results suggest that ventral P-FNs are required for normal orienting relative to airflow.
309
310 To obtain more insight into the mechanism by which ventral P-FNs control orientation, we
311 pseudorandomly introduced six stimulus perturbations throughout each 20 minute closed-loop testing
312 session (Fig. 6A). These were long (2 sec) or short (150 ms) pauses in airflow ("airflow off"), and long
313 (63.36°) or short (14.44°) angular displacements of the airflow source to the left or right (airflow "slip").
314 In response to airflow offset, control flies briefly turned towards the airflow source (Fig. 6B). When the
315 airflow resumed, flies once again turned away (see also Currier and Nagel. 2018). This sequence of
316 turns was largely intact for both long and short airflow offsets when both types of ventral P-FN were
317 silenced (Fig. 6B&C). These results suggest that, despite the abnormal orienting behavior shown by
318 ventral P-FN-silenced flies, they are still able to detect airflow and determine its direction.
319

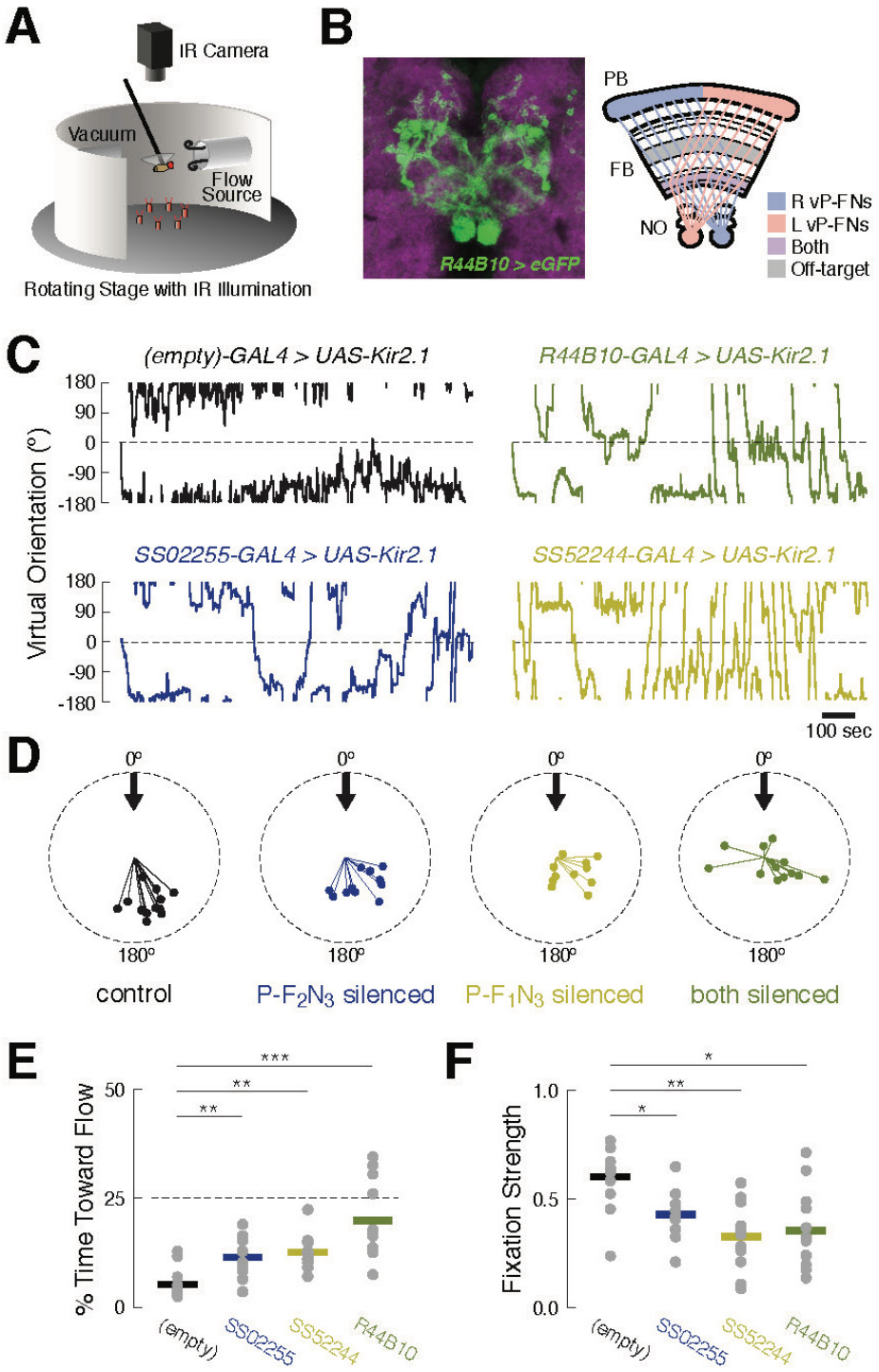

Figure 5. Silencing ventral P-FNs disrupts orientation to airflow.

(A) Schematic of flight simulator arena. Rigidly tethered flying flies orient in closed-loop with an airflow stream. Infrared illumination is used to track wingbeat angles which drive airflow rotation. The arena was otherwise in darkness. Modified from Currier and Nagel (2018).
(B) Anatomy of *R44B10-GAL4*, a driver line that targets both P-FN_2 and P-FN_3. Left: maximum z-projection of R44B10 driving *10XUAS-Kir.21-eGFP* (green). Neuropil in magenta. Right: schematic of Cx neuropils labeled by *R44B10-GAL4*. Right hemisphere ventral P-FNs (blue) target the right half of the PB, the entire FB, and the left NO. Left hemisphere ventral P-FNs (red) target the left half of the PB, the entire FB, and the right NO. Neurons from both hemispheres target all columns of FB layers 1 and 2 (purple). *R44B10-GAL4* also labels non-P-FN neurons in FB layer 5 ("off target," grey).
(C) Orientation over time for example flies of each genotype. Control flies (*empty-GAL4 > UAS-Kir2.1*, black) fixate orientations away from the airflow sources. This fixation is reduced in flies with P-FN_2 (blue), P-FN_3 (yellow) or both (dark green) silenced. The entire 20 min testing period is shown for each fly. Airflow emanated from 0° (dashed line).
(D) Stick-and-ball plots of mean orientation (ball angle) and fixation strength (stick length) for each fly tested in the airflow orienting paradigm. Fixation strength is the length of the mean orientation vector, which is inversely proportional to circular variance (see Methods). Dashed circle corresponds to perfectly consistent orienting. Thick arrow signifies the position and direction of the airflow stimulus (0°). From left to right: *(empty)-GAL4* (black, control); *SS02255-GAL4* (dark blue, P-FN_2 silenced); *SS52244-GAL4* (gold, P-FN_3 silenced); *R44B10-GAL4* (dark green, both ventral P-FNs silenced).
(E) Percentage of time each fly (gray dots) oriented toward the flow source (between +45° and -45°), as a function of genotype. Horizontal bars indicate cross-fly means, with colors as in (D). Dashed line indicates the expected value for random orienting (chance). **, $p < 0.01$; ***, $p < 0.001$ (rank-sum test).
(F) Fixation strength (as illustrated in (D)) for each fly as a function of genotype. A value of 1 indicates perfect fixation. Plot details as in (E). *, $p < 0.05$; **, $p < 0.01$ (rank-sum test).

We next wondered if the poor orienting ability of ventral P-FN-silenced flies arises from motor deficits. Our results suggest that this is not the case. We found no differences between the distributions of wingbeat angle differences for control and silenced flies (Fig. 6D). Similarly, silencing ventral P-FNs did not change the distribution of integrated turn angles following airflow direction slips (Fig. 6E). Together with our airflow offset data, these results suggest that silencing ventral P-FNs leaves both sensory and motor function intact.

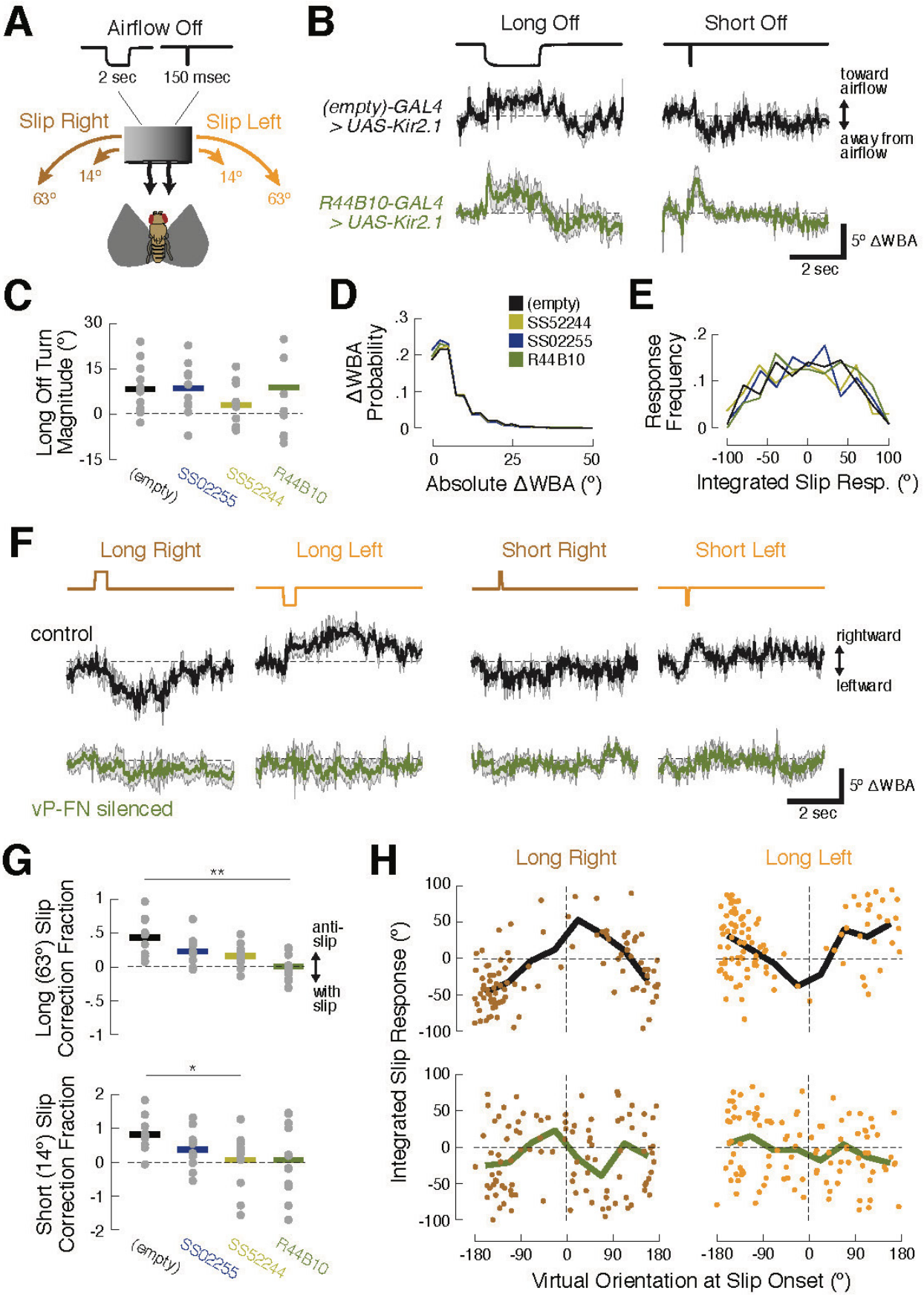
A
Airflow Off
2 sec
150 msec
Slip Right
Slip Left
14°
14°
63°
63°
B
Long Off
Short Off
(empty)-GAL4 > UAS-Kir2.1
R44B10-GAL4 > UAS-Kir2.1
toward airflow
away from airflow
5° ΔWBA
2 sec
C
Long Off Turn Magnitude (°)
(empty)
SS02255
SS52244
R44B10
D
ΔWBA Probability
(empty)
SS52244
SS02255
R44B10
Absolute ΔWBA (°)
E
Response Frequency
Integrated Slip Resp. (°)
F
Long Right
Long Left
Short Right
Short Left
control
rightward
leftward
vP-FN silenced
5° ΔWBA
2 sec
G
Long (63°) Slip Correction Fraction
anti-slip
with slip
Short (14°) Slip Correction Fraction
(empty)
SS02255
SS52244
R44B10
H
Long Right
Long Left
Integrated Slip Response (°)
Virtual Orientation at Slip Onset (°)

Figure 6. Ventral P-FNs are required to convert airflow orientation changes into heading-appropriate turns.

(A) Stimulus manipulations. Six manipulations were presented pseudo-randomly every 20 seconds during closed-loop flight: short wind offset (150 msec); long wind offset (2 sec); short (14.44º) and long (63.36º) rightward slip of virtual orientation; and short and long leftward slip of virtual orientation. Slip velocity was 144 º/sec.
(B) Responses to long and short airflow offsets in ventral P-FN-silenced flies (*R44B10-GAL4>UAS-Kir2.1*, dark green) and control flies (*empty-GAL4>UAS-Kir2.1*, black). Traces show mean +/- SEM difference in wingbeat angles (ΔWBA), a proxy for intended turning. In this plot, positive ΔWBA values indicate turns towards the airflow source and negative ΔWBA values indicate turns away from the airflow source. Dashed line represents no turning.
(C) Mean ΔWBA (integrated over 2 sec) in response to a long airflow offset for each fly (gray dots) of each genotype. Horizontal bars indicate cross-fly means. Positive ΔWBA values represent turns toward the airflow source. All groups are statistically indistinguishable by rank-sum test.
(D) Probability distributions of ΔWBA values for control (black), P-FN-silenced (gold), P-FN-silenced (dark blue), and all ventral P-FN-silenced flies (dark green). The distributions are statistically indistinguishable by KS-test.
(E) Probability distributions of integrated slip responses for each genotype (colors as in (D)). Slip responses are integrated over 5 sec of slip stimulus, with both leftward (negative) and rightward (positive) slips included. The distributions are statistically indistinguishable by KS-test.
(F) Responses to orientation slips in ventral P-FN-silenced flies (*R44B10-GAL4>UAS-Kir2.1*, dark green) and control flies (*empty-GAL4>UAS-Kir2.1*, black). In this plot, positive ΔWBA values indicate rightward turns and negative ΔWBA values indicate leftward turns. Traces show cross-fly mean +/- SEM with colors as in (B).
(G) Fraction of slip displacement corrected by each fly (gray dots) of each genotype. Values represent mean integrated slip response divided by negative slip magnitude. Positive values indicate "corrective" turns in the opposite direction of the slip. A correction fraction of 1 indicates that a fly steered the airflow direction to be identical before and after a slip trial. Note differing Y-axis scales for each plot. *, $p < 0.05$; **, $p < 0.01$ (rank-sum test).
(H) Integrated slip response (as in (E)) as a function of orientation at the time of slip onset for each long right slip (brown dots) and long left slip (orange dots). Thick lines represent the mean binned integrated slip response (45º bins), and are colored according to genotype, as in (B). Slip responses are a function of orientation in control flies, but not in ventral P-FN-silenced flies.

In contrast, silencing ventral P-FNs dramatically impaired the selection of turns following airflow direction slips. In response to slips, control flies generally made corrective turns in the direction opposite the slip (Fig. 6F, top). For rightward slips, control flies made turns to left, and for leftward slips, turns to the right. The duration and magnitude of the slip response varied with slip duration in control flies, such that turns following long slips (Fig. 6F, left) were larger than turns following short slips (Fig. 6F, right). On average, control flies' reactive turns corrected for 45% of the orientation change induced by long slips, and 90% of short slips (Fig. 6G). Conversely, flies with both types of ventral P-FNs silenced (*R44B10-Gal4>UAS-Kir2.1*) showed no turning response, on average, to slips of any direction or duration (Fig. 6F&G). When only one type of ventral P-FN was silenced, we observed a smaller reduction in mean slip responses. Together, these results suggest that ventral P-FNs may be specifically involved in generating an appropriate turning response following a change in the direction of airflow.

To examine slip correction in more detail, we plotted the integrated slip response as a function of orientation at slip onset (Fig. 6H). These plots reveal a strong relationship for control flies. When these flies were oriented approximately "with the flow" (near 180º), they tended to correct for the slip with a gain near 1. In other words, flies made turns opposite the slip direction when they were near their preferred orientation. Conversely, control flies showed no response, on average, when oriented perpendicular to the flow direction (90º or -90º). Intriguingly, in the rare event that a control fly was oriented into the flow (near 0º), they actually turned *with* the slip, perhaps because this allowed for a faster transition back to a "with the flow" preferred orientation. In flies with both types of ventral P-FNs silenced, slip responses did not depend on orientation at slip onset. These data argue that responses

351 to airflow slip depend on orientation, and support the hypothesis that ventral P-FNs are required to
352 convert airflow direction changes into heading-appropriate turning responses.
353
354
355 **Discussion**
356
357 *Organization of sensory modalities in a set of Cx columnar neurons*
358
359 All animals make use of many different sensory cues to navigate through their environments. Insects
360 and rodents use visual landmarks to return to remembered locations (Ofstad et al., 2011; Collett et al.,
361 2001; Etienne et al., 1990). Odor cues are widely used to navigate towards sources of food or mates
362 (Baker et al., 2018). Movements of the air or water are prominent cues for orientation and navigation
363 across species (Chapman et al., 2011; Alerstam et al., 2015). How neural circuits are organized to
364 process and combine these diverse cues is a fundamental question in neuroscience and evolution.
365
366 In vertebrates, several structures are known to play roles in spatial orientation and navigation. The
367 tectum, or superior colliculus, is an evolutionarily ancient structure that underlies egocentric
368 orientation to multi-modal cues. The tectum receives spatially organized information from different
369 senses in distinct layers (Knudsen, 1982; Hiramoto and Cline, 2009; Thompson et al., 2016). Alignment
370 of these sensory maps with motor maps allows for orientation to spatially localized, multi-modal cues,
371 such as prey (duLac and Knudsen, 1990; Bianco and Engert, 2015). In contrast, the hippocampus
372 exhibits multi-sensory place fields that are not anatomically organized by modality or spatial location,
373 and only indirectly drives navigation to remembered locations (O'Keefe, 1979, Redish et al., 2001).
374 Whether the insect Cx exhibits sensory responses that are organized according to modality is not
375 known.
376
377 In *Drosophila*, the development of precise genetic driver lines for targeting individual cell types has
378 allowed researchers to identify functional differences between anatomically and morphologically
379 similar cells (Wolff et al., 2015; Omoto et al., 2018). To date, most studies using these tools in the Cx
380 have focused on visual stimuli (Weir and Dickinson, 2015; Seelig and Jayaraman, 2013; Green et al.,
381 2017; Turner-Evans et al., 2017; Omoto et al., 2017, Fisher et al., 2019). Here we undertook a survey
382 of genetically identified columnar cell types in the Cx using stimuli of three different modalities
383 presented in an explicitly directional manner.
384
385 Surprisingly, we saw few directionally-tuned responses to the visual landmark, despite the fact that
386 this stimulus elicits strong orienting behavior. In contrast, we observed robust directional responses to

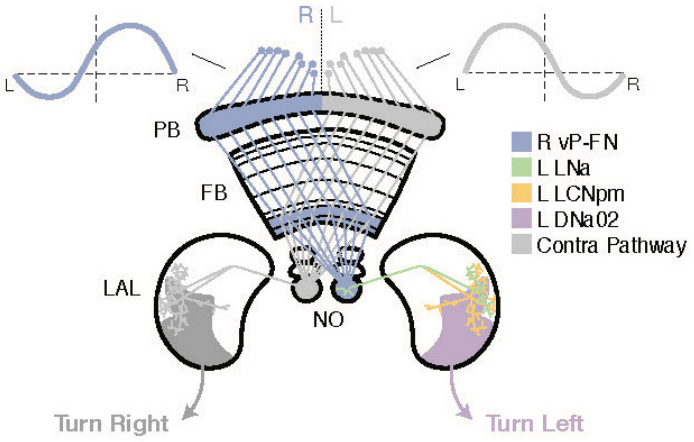

Figure 7. Hypothesized circuit promoting orientation in the direction of airflow.

A model for airflow orientation in *Drosophila*. Right hemisphere ventral P-FNs (blue) are tuned for airflow from the right, and cross to the left hemisphere NO. Using the EM hemibrain (Xu et al., 2020), we identified two targets of these cells: LNa (green), which is downstream of P-FN (PFNa in EM data), and and LCNpm (orange), which is downstream of P-FN (PFNm and PFNp in EM data). LNa and LCNpm neurons could carry contralateral airflow signals from ventral P-FNs to LAL descending neurons, such as DNa02 (purple), which is known to drive ipsilateral tuning (Rayshubskiy et al., 2020). In this model, ventral P-FNs responding to ipsilateral airflow would driving contralateral turning, allowing flies to adopt orientations aligned with the direction of airflow. The signaling pathway for left hemisphere ventral P-FNs is shown in gray. See Methods for additional details on connectomic analysis.

the airflow stimulus. These responses were strongest in neurons targeting the third nodulus compartment and the ventral layers of the fan-shaped body (ventral P-FNs). In contrast to recent studies of visual responses in the Cx (Weir and Dickinson, 2015; Shiozaki et al., 2020) the sensory responses we observed did not require flight or walking behavior. The robust airflow sensitivity of ventral P-FNs was only weakly modulated odor, and was not modulated by the visual cue. Across our surveyed cell types, we observed largely weak or inconsistent responses to an attractive odor, apple cider vinegar. This is also surprising, as a recent trans-synaptic tracing study identified the FB as a downstream target of the mushroom body, a structure known to be involved in olfactory memory (Scalpen et al., 2020). However, none of the cell types we examined innervate the dorsal portion of the FB, the primary target of the mushroom body output neurons studied so far. Whether these layers exhibit olfactory responses and participate in olfactory-driven navigation is an interesting topic for future investigations.

Robust responses to landmarks similar to our own visual stimulus have been observed in other parts of the Cx, specifically in a group of ring neurons that provide input to the EB (Seelig and Jayaraman, 2013; Sun et al., 2017; Omoto et al., 2017; Fisher et al., 2019), and in so-called “compass” neurons that connect the EB to the PB (Seelig and Jayaraman, 2015; Green et al., 2017; Fisher et al., 2019). Responses to visual motion (Weir and Dickinson, 2015), and light polarization (Heinze and Homberg, 2007; Heinze et al., 2009) are also prominent in other Cx cell types. Motor responses have also been observed in Cx neurons, including P-ENs (Green et al., 2017) and a subset of P-FNs that target the middle layers of the FB (Shiozaki et al., 2020). Steering-related responses such as these were conspicuously absent from ventral P-FNs (Shiozaki et al., 2020), which showed the most robust airflow responses in our study. Together, these studies suggest that different layers of the Cx may posses some laminar segregation of sensory modalities and motor representations, reminiscent of the vertebrate tectum.

413

414 *A mechanism for FB-driven action selection*

415

416 Although the Cx is broadly associated with navigation, the precise behavioral role that its structures
417 play is unclear. In line with previous work (Harley and Ritzmann, 2010; Martin et al., 2015), our results
418 are consistent with the FB being more directly involved in steering and action selection than other Cx
419 structures such as the EB. We have shown that two classes ventral P-FN, which are preferentially
420 sensitive to the direction of airflow, are required for stable orientation to airflow in a closed-loop flight
421 simulator. When we silenced ventral P-FNs, flies still turned toward the airflow source at flow offset,
422 suggesting that these cells are not required to detect airflow or to determine its direction. Flies with
423 silenced ventral P-FNs also exhibit a normal range of motor behavior, arguing that ventral P-FNs do
424 not generate the pool of possible responses to changing airflow direction. Instead, our data suggest
425 that ventral P-FNs guide selection from this pool, specifically converting mechanically detected
426 changes in orientation into a heading-appropriate turning response. These results broadly support the
427 idea that the FB plays a role in action selection, and provide new details about how this selection
428 occurs for a particular sensory cue.

429

430 How might ventral P-FNs achieve this function? We have shown that ventral P-FNs with cell bodies in
431 the left hemisphere are excited by airflow from the left, and vice-versa for right hemisphere neurons. In
432 order to produce corrective turns that stabilize orientation away from an airflow source, activation of
433 left-hemisphere ventral P-FNs should drive turns to the right, while activation of right-hemisphere
434 ventral P-FNs should drive turns to the left. Ventral P-FNs make most of their outputs within the FB
435 and NO (Franconville et al., 2018), and P-FNs in a given hemisphere target the NO on the opposite
436 side (Fig. 7; Wolff and Rubin, 2015). A simple query of the hemi-brain connectome (Xu et al., 2020)
437 reveals that major downstream targets of P-F_2N_3 and P-F_1N_3 neurons are LNa and LCNpm neurons,
438 respectively (Fig. 7). Both of these cell types connect one hemisphere's NO to the Lateral Accessory
439 Lobe (LAL) on the same side of the brain. Thus, right-hemisphere ventral P-FNs provide output to the
440 left-hemisphere LAL, and vice-versa. Because activation of LAL descending neurons has been shown
441 to produce ipsilateral turns (Rayshubskiy et al., 2020), this ventral P-FN—contralateral LAL connection
442 could provide one pathway for ventral P-FNs to elicit corrective turns that stabilize with-flow
443 orientation.

444

445 However, our data also suggest that turns following airflow direction changes depend on a fly's
446 heading with respect to airflow. How might heading information be integrated with ventral P-FN
447 activity? One possibility is that ventral P-FNs receive a heading signal from compass neurons via the
448 PB (Franconville et al., 2018; Turner-Evans et al., 2017; Green et al., 2017). Although a recent study of

visual orientation found that ventral P-FNs contain no heading information (Shiozaki et al., 2020), such a signal could emerge during closed-loop navigation specifically with an airflow stimulus. An important future question is what kind of information is represented in ventral P-FNs during closed-loop navigation relative to airflow.

The role of ventral P-FNs in natural behavior

Although we have shown that silencing ventral P-FNs impairs airflow orientation in a tethered flight paradigm, how this finding might translate to free flight is unclear. Insects are often transported on the wind during free flight (Reynolds et al., 2010; Leitch et al., 2020), generating a strong optic flow signal (Mronz and Lehman, 2008; Theobald et al., 2010) rather than a persistent mechanosensory signal, as investigated in this study. Although steady-state wind direction may not be detected by mechanoreceptors, evidence suggests that the antennae can respond to transient gusts, or changes, in wind direction (Fuller et al., 2014). Multiple species of flying insects can orient to airflow in tethered flight, with many adopting “downwind” orientations like those we have seen (Kaushik et al., 2020; Currier and Nagel, 2018). Our results suggest that flies achieve this orientation in part by responding to transient changes in the airflow direction with heading-appropriate corrective turns. Because this mechanism relies on transient detection of airflow, it could play a role in free flight. Silencing experiments in a wind tunnel (van Breugel et al., 2014) will be required to test this hypothesis directly.

Our results raise the question of whether ventral P-FNs might respond to other cues, such as optic flow, that could also signal the presence and direction of wind. Although we did not investigate responses to optic flow in this study, a prior imaging study found that the ventral FB responds to regressive visual motion (Weir and Dickinson, 2015). Future experiments could examine ventral P-FN responses to both optic flow and airflow in order to address whether these cells respond specifically to one modality, or to a more abstract quantity, such as physical displacement, which generates both signals.

A related question is how navigational drives from different modalities interact. Work in desert ants and dung beetles has identified an apparent sensory hierarchy during navigation, where wind cues are often ignored if visual cues are present and reliable (Müller and Wehner, 2007; Dacke et al., 2019). However, airflow-based turn drives can also be summed with vision-based turn drives (Currier and Nagel, 2018; Budick et al., 2007) or can be gated by olfactory cues (Alvarez-Salvado et al., 2018; van Breugel et al., 2014). Sensory context and recent sensory experience are also known to have immediate impacts on the activity of Cx neurons (Shiozaki et al., 2020; Fisher et al., 2019). Our work

identifying the ventral FB as a locus for airflow-guided orientation provides an entry-point for studying the role of the Cx in such multi-modal interactions.

Finally, our observation that ventral P-FNs are required to correct for slips in airflow direction is reminiscent of another study (Green et al., 2019), which found that EB compass neurons are required for flies to correct for visual target orientation jumps. The reduced orientation stability of our ventral P-FN-silenced flies also echoes the unstable walking trajectories of flies with silenced compass neurons. Green et al. additionally found that chemogenetically jumping the EB heading representation resulted in corrective turns. LAL descending neurons respond during this kind of corrective turn (Rayshubskiy et al., 2020), and the LAL is a likely target of ventral P-FNs (Fig. 7). One hypothesis consistent with these findings is therefore that different regions of the EB and FB encode distinct and potentially competitive sensory stimuli that converge at the level of the LAL, allowing the fly to select a single orientation. Alternatively, competition between different orienting cues might be resolved by local interactions within the Cx itself. Identifying the loci that compare and combine turning drives from these discrete systems will be a major step toward understanding flexible navigation in real-world, multi-sensory environments.

Acknowledgements

We would like to thank Michael Reiser for flies and members of the Nagel and Schoppik labs for feedback and helpful discussion. This work was supported by grants from the NIH (R01DC017979 and R01MH109690), and NSF (IOS-1555933) KIN, a McKnight Scholar Award to KIN, and a New York University Dean's Fellowship to TAC.

Author Contributions

Conceptualization — TAC & KIN; Methodology — TAC & KIN; Software — TAC; Investigation — TAC; Validation — TAC & AMMM; Formal Analysis — TAC & AMMM; Writing - Original Draft — TAC; Writing - Review & Editing — TAC, AMMM & KIN; Supervision — KIN; Funding Acquisition — TAC & KIN.

Declaration of Interests

The authors declare no competing interests.

521 **References**

522

523

524 Alerstam, T., Chapman, J.W., Ba, J., Nilsson, C., Smith, A.D., Reynolds, D.R., Klaassen, R.H.G., and
525 Hill, J.K. (2011). Convergent patterns of long-distance nocturnal migration in noctuid moths and
526 passerine birds. Proc R Soc B 278, 3074–3080.

527

528 Álvarez-Salvado, E., Licata, A.M., Connor, E.G., Mchugh, M.K., King, B.M.N., Stavropoulos, N., Victor,
529 J.D., Crimaldi, J.P., and Nagel, K.I. (2018). Elementary sensory-motor transformations underlying
530 olfactory navigation in walking fruit-flies. eLife 7, e37815.

531

532 Baker, K.L., Dickinson, M., Findley, T.M., Gire, D.H., Louis, M., Suver, M.P., Verhagen, J. V, Nagel, K.I.,
533 and Smear, M.C. (2018). Algorithms for Olfactory Search across Species. J Neurosci 38, 9383–9389.

534

535 Bianco, I.H., and Engert, F. Visuomotor Transformations Underlying Hunting Behavior in Zebrafish.
536 Curr Biol 25, 831–846.

537

538 Budick, S.A., Reiser, M.B., and Dickinson, M.H. (2007). The role of visual and mechanosensory cues in
539 structuring forward flight in Drosophila melanogaster. J. Exp. Biol. 210, 4092–4103.

540

541 Cardé, R.T., and Willis, M.A. (2008). Navigational Strategies Used by Insects to Find Distant, Wind-
542 Borne Sources of Odor. J Chem Ecol 34, 854–866.

543

544 Collett, T.S., Collett, M., and Wehner, R. (2001). Guidance of desert ants by extended landmarks. J
545 Exp Biol 204, 1635–1639.

546

547 Currier, T.A., and Nagel, K.I. (2018). Multisensory Control of Orientation in Tethered Flying Drosophila.
548 Curr. Biol. 28, 1–14.

549

550 Dacke, M., Bell, A.T.A., Foster, J.J., Baird, E.J., Strube-bloss, M.F., and Byrne, M.J. (2019). Multimodal
551 cue integration in the dung beetle compass. PNAS 116, 14248–14253.

552

553 du Lac, S., and Knudsen, E.I. (1990). Neural maps of head movement vector and speed in the optic
554 tectum of the barn owl. J Neurophysiol 63, 131–146.

555

556 Etienne, A.S., Teroni, E., Hurni, C., and Portenier, V. (1990). The effect of a single light cue on homing
557 behaviour of the golden hamster. Animal Behaviour 39, 17–41.
558
559 Fisher, Y.E., Lu, J., Alessandro, I.D., and Wilson, R.I. (2019). Sensorimotor experience remaps visual
560 input to a heading-direction network. Nature 576, 121–125.
561
562 Franconville, R., Beron, C., and Jayaraman, V. (2018). Building a functional connectome of the
563 Drosophila central complex. eLife 7, e37017.
564
565 Fuller, S.B., Straw, A.D., Peek, M.Y., Murray, R.M., and Dickinson, M.H. (2014). Flying Drosophila
566 stabilize their vision-based velocity controller by sensing wind with their antennae. PNAS 111, 1182–
567 1191.
568
569 Giraldo, Y.M., Leitch, K.J., Ros, I.G., Warren, T.L., Weir, P.T., and Dickinson, M.H. (2018). Sun
570 Navigation Requires Compass Neurons in Drosophila. Curr. Biol. 28, 2845-2852.e4.
571
572 Gire, D.H., Kapoor, V., Arrighi-allisan, A., Seminara, A., and Murthy, V.N. (2016). Mice Develop Efficient
573 Strategies for Foraging and Navigation Using Complex Natural Stimuli. Curr. Biol. 26, 1261–1273.
574
575 Goodman, M.B., and Lockery, S.R. (2000). Pressure polishing: a method for re-shaping patch pipettes
576 during fire polishing. J Neurosci Meth 100, 13–15.
577
578 Green, J., Adachi, A., Shah, K.K., Hirokawa, J.D., Magani, P.S., and Maimon, G. (2017). A neural
579 circuit architecture for angular integration in Drosophila. Nature 546, 101–106.
580
581 Green, J., Vijayan, V., Pires, P.M., Adachi, A., and Maimon, G. (2019). A neural heading estimate is
582 compared with an internal goal to guide oriented navigation. Nat Neurosci 22, 1460–1468.
583
584 Hanesch, U., Fischbach, K.F., and Heisenberg, M. (1989). Neuronal architecture of the central
585 complex in Drosophila melanogaster. Cell Tissue Res. 257, 343–366.
586
587 Harley, C.M., and Ritzmann, R.E. (2010). Electrolytic lesions within central complex neuropils of the
588 cockroach brain affect negotiation of barriers. J Exp Biol 213, 2851–2864.
589
590 Heinze, S., Gotthardt, S., and Homberg, U. (2009). Transformation of Polarized Light Information in the
591 Central Complex of the Locust. J. Neurosci. 29, 11783–11793.

Heinze, S., and Homberg, U. (2007). Maplike Representation of celestial E-vector orientations in the brain of an insect. Science 431, 2004–2006.

Heisenberg, M., and Wolf, R. (1979). On the fine structure of yaw torque in visual flight orientation of Drosophila melanogaster. J. Comp. Physiol. 130, 113–130.

Hiramoto M., and Cline, H.T. (2009). Convergence of multisensory inputs in Xenopus tadpole tectum. Dev Neurobiol 69, 959–971.

Holland, R.A., Thorup, K., Gagliardo, A., Bisson, I.A., Knecht, E., Mizrahi, D., and Wikelski, M. (2009). Testing the role of sensory systems in the migratory heading of a songbird. J Exp Biol 212, 4065–4071.

Kathman, N.D., and Fox, J.L. (2019). Representation of Haltere Oscillations and Integration with Visual Inputs in the Fly Central Complex. J Neurosci 39, 4100–4112.

Kaushik, P.K., Renz, M., and Olsson, S.B. (2020). Characterizing long-range search behavior in Diptera using complex 3D virtual environments. PNAS 117, 12201–12207.

Knudsen, I.E. (1982). Auditory and visual maps of space in the optic tectum of the owl. J Neurosci 2, 1177–1194.

Leitch, K., Ponce, F., van Breugel, F., and Dickinson, M.H. (2020). The long-distance flight behavior of Drosophila suggests a general model for wind-assisted dispersal in insects. bioRxiv, 2020.06.10.145169.

Lockery, S.R. (2011). The computational worm: Spatial orientation and its neuronal basis in C. elegans. Curr. Opin. Neurobiol. 21, 782–790.

Maimon, G., Straw, A.D., and Dickinson, M.H. (2008). A Simple Vision-Based Algorithm for Decision Making in Flying Drosophila. Curr. Biol. 18, 464–470.

Martin, J.P., Guo, P., Mu, L., Harley, C.M., and Ritzmann, R.E. (2015). Central-complex control of movement in the freely walking cockroach. Curr. Biol. 25, 2795–2803.

Montgomery, J.C., Baker, C.F., and Carton, A.G. (1997). The lateral line can mediate rheotaxis in fish. Nature 389, 960–963.

Mronz, M., and Lehmann, F. (2008). The free-flight response of Drosophila to motion of the visual environment. J Exp Biol 211, 2026–2045.

Müller, M., and Wehner, R. (2007). Wind and sky as compass cues in desert ant navigation. Naturwissenschaften 94, 589–594.

Nagel, K.I., and Wilson, R.I. (2016). Mechanisms Underlying Population Response Dynamics in Inhibitory Interneurons of the Drosophila Antennal Lobe. J. Neurosci. 36, 4325–4338.

Neuser, K., Triphan, T., Mronz, M., Poeck, B., and Strauss, R. (2008). Analysis of a spatial orientation memory in Drosophila. Nature 453, 1244–1247.

Ofstad, T.A., Zuker, C.S., and Reiser, M.B. (2011). Visual place learning in Drosophila melanogaster. Nature 474, 204–209.

O'Keefe, J. (1979). A review of hippocampal place cells. Prog Neurobiol 13, 419–439.

Omoto, J.J., Keleş, M.F., Nguyen, B.C.M., Bolanos, C., Lovick, J.K., Frye, M.A., and Hartenstein, V. (2017). Visual Input to the Drosophila Central Complex by Developmentally and Functionally Distinct Neuronal Populations. Curr. Biol. 27, 1098–1110.

Omoto, J.J., Nguyen, B.M., and Kandimalla, P. (2018). Neuronal Constituents and Putative Interactions Within the Drosophila Ellipsoid Body Neuropil. Front Neural Circuits 12, 1–26.

Phillips-Portillo, J. (2012). The central complex of the flesh fly, Neobellieria bullata: Recordings and morphologies of protocerebral inputs and small-field neurons. J. Comp. Neurol. 520, 3088–3104.

Redish, A.D., Battaglia, F.P., Chawla, M.K., Ekstrom, A.D., Gerrard, J.L., Lipa, P., Rosenzweig, E.S., Worley, P.F., Guzowski, J.F., McNaughton, B.L., and Barnes, C.A. (2001). Independence of firing correlates of anatomically proximate hippocampal pyramidal cells. J Neurosci 21, RC134.

Reichardt, W., and Poggio, T. (1976). Visual control of orientation behavior in the fly. Part I: A quantitative analysis. Q Rev Biophys 9, 311–375.

Reynolds, A.M., Reynolds, D.R., Smith, A.D., and Chapman, J.W. (2010). A single wind-mediated mechanism explains high-altitude 'non-goal oriented' headings and layering of nocturnally migrating insects. Proc R Soc B 277, 765–772.

Ritzmann, R.E., Ridgel, A.L., and Pollack, A.J. (2008). Multi-unit recording of antennal mechano-sensitive units in the central complex of the cockroach, Blaberus discoidalis. J. Comp. Physiol. A 194, 341–360.

Scaplen, K.M., Talay, M., Nunez, K.M., Salamon, S., Waterman, A.G., Gang, S., Song, S.L., Barnea, G., and Kaun, K.R. (2020). Circuits that encode and guide alcohol-associated preference. eLife 9, e48730.

Seelig, J.D., and Jayaraman, V. (2013). Feature detection and orientation tuning in the Drosophila central complex. Nature 503, 262–266.

Seelig, J.D., and Jayaraman, V. (2015). Neural dynamics for landmark orientation and angular path integration. Nature 521, 186–191.

Shiozaki, H.M., Ohta, K., and Kazama, H. (2020). A Multi-regional Network Encoding Heading and Steering Maneuvers in Drosophila. Neuron 106, 1–16.

Stone, T., Webb, B., Adden, A., Weddig, N. Ben, Honkanen, A., Templin, R., Wcislo, W., Scimeca, L., Warrant, E., and Heinze, S. (2017). An Anatomically Constrained Model for Path Integration in the Bee Brain. Curr. Biol. 27, 3069-3085.e11.

Strauss, R., and Heisenberg, M. (1993). A Higher Control Center of Locomotor Behavior in the Drosophila Brain. J. Neurosci. 13, 1852–1861.

Suli, A., Watson, G.M., Rubel, E.W., and Raible, D.W. (2012). Rheotaxis in Larval Zebrafish Is Mediated by Lateral Line Mechanosensory Hair Cells. PLoS ONE 7, e29727.

Sun, Y., Nern, A., Franconville, R., Dana, H., Schreiter, E.R., Looger, L.L., Svoboda, K., Kim, D.S., Hermundstad, A.M., and Jayaraman, V. (2017). Neural signatures of dynamic stimulus selection in Drosophila. Nat. Neurosci. 20, 1104–1113.

Suver, M.P., Matheson, A.M.M., Sarkar, S., Damiata, M., Schoppik, D., and Nagel, K.I. (2019). Encoding of Wind Direction by Central Neurons in Drosophila. Neuron 102, 828-842.

Theobald, J.C., Ringach, D.L., and Frye, M.A. (2010). Dynamics of optomotor responses in Drosophila to perturbations in optic flow. J Exp Biol 213, 1366–1375.

Thompson, A.W., Vanwalleghem, G.C., Heap, L.A., and Scott, E.K. (2016). Functional Profiles of Visual- , Auditory- , and Water Flow-Responsive Neurons in the Zebrafish Tectum. Curr. Biol. 26, 743–754.

Turner-Evans, D., Wegener, S., Rouault, H., Franconville, R., Wolff, T., Seelig, J.D., Druckmann, S., and Jayaraman, V. (2017). Angular velocity integration in a fly heading circuit. Elife 6, e23496.

Van Breugel, F., and Dickinson, M.H. (2014). Plume-tracking behavior of flying Drosophila emerges from a set of distinct sensory-motor reflexes. Curr. Biol. 24, 274–286.

Weir, P.T., and Dickinson, M.H. (2015). Functional divisions for visual processing in the central brain of flying Drosophila. PNAS 112, 5523–5532.

Wilson, R.I., and Laurent, G. (2005). Role of GABAerginc inhibition in shaping odor-evoked spatiotemporal patterns in the Drosophila antennal lobe. J Neurosci 25, 9069–9079.

Wolff, T., Iyer, N.A., and Rubin, G.M. (2015). Neuroarchitecture and neuroanatomy of the Drosophila central complex: A GAL4-based dissection of protocerebral bridge neurons and circuits. J. Comp. Neurol. 523, 997–1037.

Wolff, T., and Rubin, G.M. (2018). Neuroarchitecture of the Drosophila central complex : A catalog of nodulus and asymmetrical body neurons and a revision of the protocerebral bridge catalog. J Comp Neurol 526, 2585–2611.

Xu, C.S., Januszewski, M., Lu, Z., Takemura, S., Hayworth, K.J., Huang, G., Shinomiya, K., Maitin-Shepard, J., Ackerman, D., Berg, S., et al. (2020). A Connectome of the Adult Drosophila Central Brain. bioRxiv, 2020.01.21.911859.

Yorozu, S., Wong, A., Fischer, B.J., Dankert, H., Kernan, M.J., Kamikouchi, A., Ito, K., and Anderson, D.J. (2009). Distinct sensory representations of wind and near-field sound in the Drosophila brain. Nature 458, 201–205.

Yu, Y.S.W., Graff, M.M., Bresee, C.S., Man, Y.B., and Hartmann, M.J.Z. (2016a). Whiskers aid anemotaxis in rats. Sci Adv 2, e1600716.

Yu, Y.S.W., Graff, M.M., and Hartmann, M.J.Z. (2016b). Mechanical responses of rat vibrissae to airflow. J Exp Biol 219, 937–948.

Methods

CONTACT FOR REAGENT AND RESOURCE SHARING

Further information and requests for resources and reagents should be directed to and will be fulfilled by the Lead Contact, Katherine Nagel (katherine.nagel@nyumc.org).

EXPERIMENTAL MODEL AND SUBJECT DETAILS

Fly Stocks

All flies were raised at 25ºC on a cornmeal-agar medium under a 12-hour light/dark cycle. Flies for patch experiments were aged 1-3 days after eclosion before data collection, and flies for behavior experiments were aged 3-5 days. All data shown are from female flies. Parental stocks can be found in the key resources table. Specific genotypes presented in each figure panel are shown below. SS lines contain genetic inserts on chromosomes II and III — the transgenes occupying the second copies of these chromosomes are shown in parenthesis.

Genotype	*N*	Description	Figure Panels
w; SS52244-GAL4/(+; 10xUAS-syn21-GFP)	6	P-F_1N_3 patch line	1D,E,G,H
w; SS02255-GAL4/(+; 10xUAS-syn21-GFP)	6	P-F_2N_3 patch line	1C,E,G,H
w; SS00078-GAL4/(+; 10xUAS-syn21-GFP)	14	P-F_3N_{2d} patch line	1E-H
w; SS52577-GAL4/(+; 10xUAS-syn21-GFP)	4	P-F_3N_{2v} patch line	1E,G,H
w; SS54295-GAL4/(+; 10xUAS-syn21-GFP)	4	P-EN_1(1) patch line	1E,G,H
w; +; R12D09-GAL4/10xUAS-syn21-GFP	6	P-EN_1(2) patch line	1C,E,G,H
w; SS02239-GAL4/(+; 10xUAS-syn21-GFP)	8	P-F_3LC patch line	1C,E,G,H
w; SS54549-GAL4/(+; 10xUAS-syn21-GFP)	6	P-$F_{3\text{-}5}$R patch line	1E,G,H
w; SS52244-GAL4/(+; 10xUAS-syn21-GFP)	6	P-F_1N_3 patch line	2A
w; SS02255-GAL4/(+; 10xUAS-syn21-GFP)	6	P-F_2N_3 patch line	2A
w; SS00078-GAL4/(+; 10xUAS-syn21-GFP)	14	P-F_3N_{2d} patch line	2A,B-E
w; SS52577-GAL4/(+; 10xUAS-syn21-GFP)	4	P-F_3N_{2v} patch line	2A
w; SS54295-GAL4/(+; 10xUAS-syn21-GFP)	4	P-EN_1(1) patch line	2A
w; +; R12D09-GAL4/10xUAS-syn21-GFP	5	P-EN_1(2) patch line	2A,B-E

w; SS02239-GAL4/(+; 10xUAS-syn21-GFP)	8	P-F_3LC patch line	2A
w; SS54549-GAL4/(+; 10xUAS-syn21-GFP)	6	P-$F_{3\text{-}5}$R patch line	2A
w; SS02255-GAL4/(+; 10xUAS-syn21-GFP)	6	P-F_2N_3 patch line	3A-G
w; SS52244-GAL4/(+; 10xUAS-syn21-GFP)	6	P-F_1N_3 patch line	3H,I
w; SS02255-GAL4/(+; 10xUAS-syn21-GFP)	12	P-F_2N_3 patch line	4B-K
w; +; R44B10-GAL4/13xUAS-Kir2.1-eGFP	12	Ventral P-FN silencing line	5B-F
w; +; (empty)-GAL4/13xUAS-Kir2.1-eGFP	12	Silencing control line	5C-F
w; SS02255-GAL4/(+; 13xUAS-Kir2.1-eGFP)	11	P-F_2N_3 silencing line	5D-F
w; SS52244-GAL4/(+; 13xUAS-Kir.21-eGFP)	11	P-F_1N_3 silencing line	5D-F
w; +; R44B10-GAL4/13xUAS-Kir2.1-eGFP	12	Ventral P-FN silencing line	6B-H
w; +; (empty)-GAL4/13xUAS-Kir2.1-eGFP	12	Silencing control line	6B-H
w; SS02255-GAL4/(+; 13xUAS-Kir2.1-eGFP)	11	P-F_2N_3 silencing line	6C-E,G,H
w; SS52244-GAL4/(+; 13xUAS-Kir.21-eGFP)	11	P-F_1N_3 silencing line	6C-E,G,H

METHOD DETAILS

Electrophysiology

Flies were prepared for electrophysiology (Figs. 1-4) by tethering them to a custom fly holder and reservoir (modified from Weir et al., 2014, see supplemental files for fly holder schematic). All flies were cold anesthetized on ice for approximately 5 minutes during tethering. During anesthesia, we removed the front pair of legs from each fly to prevent disruption of electrophysiology data. We then used UV glue (KOA 30, Kemxert) to fix flies to the holder by the posterior surface of the head and the anterior-dorsal thorax. Once flies were secured, they were allowed to recover from anesthesia for 30-45 minutes in a humidified chamber at 25°C. Prior to patching, we filled the fly holder reservoir with Drosophila saline (Wilson and Laurent, 2005) and dissected away the cuticle on the posterior surface of the head, removing trachea and fat lying over the posterior surface of the brain.

Tethered and dissected flies were then placed in a custom stimulus arena on a floating table (Technical Manufacturing Corporation, 63-541) with a continuous flow of room-temperature *Drosophila* saline over the exposed brain. Briefly, *Drosophila* saline contained 103 mM sodium chloride, 3 mM potassium chloride, 5 mM TES, 8 mM trehalose dihydrate, 10 mM glucose, 26 mM sodium bicarbonate, 1 mM sodium phosphate monohydrate, 1.5 mM calcium chloride dihydrate, and 4 mM magnesium chloride hexahydrate. The solution was adjusted to a pH of 7.2 and an osmolarity of 272 mOsm.

Brains were imaged under 40X magnification (Olympus, LUMPLFLN40XW) by a microsocope (Sutter, WI-SRE3) controlled by a micromanipulator (Sutter, MPC-200). Real-time brain images were captured by a camera (Dage-MTI, IR-1000) and sent to an LCD monitor (Samsung, SMT-1734). Target neurons were identified based on expression of cytoplasmic GFP (see “Fly Stocks” above). Fluorescent stimulation was provided by an LED light source and power controller (Cairn Research, MONOLED). A dichroic/filter cube (Semrock, M341523) allowed for stimulation and emission imaging through the same objective.

We first cleared away the neural sheath overlaying target neurons by puffing 0.5% collagenase-IV (Worthington, 43E14252) through a micropipette (World Precision Instruments, TW150-3) and applying gentle mechanical force. Cell bodies overlaying target somata were then removed via gentle suction, if necessary. Once target neurons were cleaned of debris, we used fire-polished micropipettes (Goodman and Lockery, 2000) to record one neuron per fly. Prior to use, pipettes (World Precision Instruments, 1B150F-3) were pulled (Sutter, Model P-1000 Micropipette Puller) and transferred to a polishing station equipped with an inverted light microscope and a pressurized micro-forge (Scientific Instruments, CPM-2). Pipettes were polished to a tip diameter of 0.5-2 μm and an impedance of 6-12 MΩ, depending on the target cell type. Patch pipettes were filled with potassium-aspartate intracellular solution (Wilson and Laurent, 2005), which contained 140 mM of potassium hydroxide, 140 mM of aspartic acid, 10 mM of HEPES, 1 mM of EGTA, 1 mM of potassium chloride, 4 mM of magnesium adenosine triphosphate, and 0.5 mM of trisodium guanine triphosphate. We also added 13 mM of biocytin hydrazide to the intracellular solution for post-hoc labeling of recorded neurons. The solution was adjusted to a pH of 7.2 and an osmolarity of 265 mOsm. Before use, we filtered this intracellular solution with a syringe-tip filter (0.22 micron pore size, Millipore Millex-GV).

Recorded neurons were confirmed to be of the targeted type in three ways: (1) presence of a fluorescent membrane “bleb” inside the pipette after sealing onto the cell; (2) loss of cytoplasmic GFP through diffusion over the course of the recording session; (3) post-hoc biocytin fill label matching the known anatomical features of the targeted cell type. Two of these three criteria must have been met in order for a patched neuron to be considered a member of a given cell type.

Hardware for electrophysiology was adapted from one previously used (Nagel and Wilson, 2016). In brief, recorded signals passed through a headstage (Axon Instruments, CV 203BU), a pre-amp (Brownlee Precision, Model 410), and an amplifier (Molecular Devices, Axopatch 200B) before being digitized for storage (National Instruments, BNC-2090A) and gain-corrected. Data was collected at 10,000 Hz.

After all electrophysiology experiments, we removed flies from their holders and dissected out their central brains. Dissected tissue was then fixed in 4% paraformaldehyde for 14 minutes at room temperature. Fixed tissue was stored at 4ºC for up to 4 weeks before further processing (see “Immunohistochemistry,” below).

Stimulus Delivery

Once an active recording was obtained, we presented a series of sensory stimuli from multiple directions. Stimulus delivery was achieved by a modified version of a perviously used system (Currier and Nagel, 2018). Briefly, custom LabView (National Instruments) software controlled the tiggering of airflow (25 cm/s), odor (20% apple cider vinegar), and/or ambient illumination (15 μW/cm^2) of a high contrast vertical bar that subtended approximately 30° of visual angle. Stimulus intensities for airflow, odor, and light were measured with a hot-wire anemometer (Dantec Dynamics MiniCTA 54T42), a photo-ionization detector (Aurora Scientific, miniPID 200B), and a power meter (ThorLabs, PM 100D and S130C), respectively. All stimuli emanated from the same location in the arena, and the entire arena could be rotated with a stepper motor (Oriental Motor, CVK564FMBK) around the stationary fly. This setup allowed us to present cues from any arbitrary direction. Rotations of the motor were slow (20°/s) and driven at minimal power to minimize vibration and electromagnetic disturbances.

For our initial survey of CX columnar neurons (Figs. 1-3), we used a pseudorandom session design broken down by stimulus direction (-90°, 0°, 90° and 180°) and type (stripe only, airflow only, airflow & stripe together, airflow & odor together, or all 3 stimuli simultaneously). Each 12-second trial included 4 sec of pre-stimulus baseline, 4 sec of stimulus presentation, and 4 sec of post-stimulus time. The first 1 sec of each trial's baseline period included a 500 ms injection of -2 pA to monitor input resistance over time (this period is not plotted in any Figures). Between trials, a 9-second inter-trial-interval allowed the cell to rest while the motor rotated the arena to the next trial's stimulus direction. All 20 unique combinations of stimulus direction and condition were presented 4 times each, and each stimulus was presented before the next round of repetitions began. The total session recording time was approximately 50 minutes. If cell health was observed to decay before the session was complete, data was discarded after the preceding "set" of 20 stimuli. For a cell to be included in the survey, at least 40 trials (2 sets of repetitions) must have been completed. Of the 52 neurons patched in the survey, 46 remained healthy for all 80 trials.

To investigate how airflow responses varied by column (Fig. 4), we used 8 directions (-135°, -90°, -45°, 0°, 45°, 90°, 135°, 180°) and presented only the airflow stimulus. Trial and pseudorandom session design were the same as above, but we increased the number of stimulus repetitions to 5, for a total of 40 trials. All 12 flies in this dataset completed all 40 trials.

Immunohistochemistry

Fixed brains were processed using standard immunohistochemistry protocols. Briefly, we blocked for 30 minutes at room temperature in phosphate buffered saline (PBS, Sigma, P5493-1L) containing 5% normal goat serum (Vector Laboratories, S-1000) and 0.1% Triton X-100 (Sigma, X100-100ML). The primary antibody solution was identical to the blocking solution, but had a 1:50 dilution of rabbit anti-GFP antibodies (Fisher Scientific, A-6455) and a 1:50 dilution of mouse anti-bruchpilot antibodies (Developmental Studies Hybridoma Bank,

nc82-s). The secondary antibody solution was similarly based on the blocking solution, but also contained a 1:250 dilution of alexa488-conjugated goat anti-rabbit anitbodies (Fisher Scientific, A-11034), a 1:250 dilution of alex633-conjugated goat anti-mouse antibodies (Fisher Scientific, A-21052), and a 1:1000 dilution of alexa568-conjugated streptavidin (Fisher Scientific, S-11226). Antibody incubations were for 24 hours at room temperature. We washed brains in 0.1% PBS-Triton three times for 5 minutes after each antibody phase. Immuno-processed brains were mounted on slides (Fisher Scientific, 12-550-143 and 12-452-C) and imaged under a confocal fluorescence microscope (Zeiss, LSM 800) at 20X magnification (Zeiss, W Plan-Apochromat 20x).

Behavior

For flight simulator experiments (Figs. 5&6) we fixed flies in place using rigid tungsten tethers (see Currier and Nagel, 2018). All flies were cold anesthetized for approximately 5 minutes during the tethering process. During anesthesia, a drop of UV-cured glue was used to tether the notum of anesthetized flies to the end of a tungsten pin (A-M Systems, # 716000). Tethered flies' heads were therefore free to move. We additionally removed the front pair of legs from each fly to prevent disruption of wing tracking (see below). Flies were then allowed to recover from anesthesia for 30-60 minutes in a humidified chamber at 25°C before behavioral testing.

Tethered behavior flies were placed one at a time in a custom stimulus arena described in a previous paper (Currier and Nagel, 2018). The dark arena was equipped with a pair of tubes (one flow, one suction) that could create a constant stream of airflow over the fly. A camera (Allied Vision, GPF031B) equipped with a zoom lens (Edmund Optics, 59-805) and infrared filter (Midwest Optical, BP805-22.5) was used to capture images of the fly in real-time. Custom LabView software was used to detect the angle of the leading edge of each wing. We multiplied the difference between these wing angles (ΔWBA) by a static, empirically verified gain (0.04, see Currier and Nagel, 2018) to determine each fly's intended momentary angular velocity. This signal was sent to a stepper motor (Oriental Motor, CVK564FMAK) which rotated the airflow tubes around the fly. The difference in wingbeat angles and integrated heading were also saved for later analysis. This process was repeated at 50 Hz.

Each fly's 20-minute behavioral testing session was broken down into 20-sec trials that began with a manipulation to the airflow stimulus. Air flowed continuously throughout the entire session, except when interrupted as a stimulus manipulation. We used two durations of airflow offset: 2 samples (100 ms) and 100 samples (2 sec). Additional manipulations included open-loop (not fly-controlled) rotations of the airflow tubes to the left or right of its current position. These open-loop rotations were driven continuously at the maximum speed of the motor (144 °/s) for either 5 samples (14.4°) or 22 samples (63.36°). This gave four additional manipulations: long and short rotations to the left and right. These six stimulus manipulations were pseudorandomly presented ten times each. All flies shown in Figs. 5&6 completed all 60 trials.

QUANTIFICATION AND STATISTICAL ANALYSIS

Analysis of Physiology Data

All data was processed in MATLAB (Mathworks, version 2017B) with custom analysis scripts. Spike times were found by first high-pass filtering the raw membrane potential signal with a second order Butterworth filter (40 Hz cutoff frequency) and then identifying cell type-specific threshold crossings. We used the -2pA test pulse at the beginning of each trial to calculate and track input resistance over time (Fig. S1D).

To calculate membrane potential and spiking responses to our stimuli, we first defined the baseline period for each trial as a 1-second long data segment ending 500 ms before stimulus onset. We additionally defined a response period, which began 500 ms after stimulus onset and similarly lasted 1 sec. Spiking and membrane potential responses in each trial were defined as the mean firing rate or membrane potential during the response period minus the mean of the baseline period. Mean responses (Figs. 1-4 and S2) for each cell to each stimulus were calculated by averaging these responses to stimulus repetitions.

Cross-condition correlation coefficients (Figs. 2,3 and S3) were found by first taking the mean PSTH across stimulus repeats in each stimulus condition. PSTHs were found by convolving spike trains with a 1 sec Hanning window. We next truncated this full trial mean data to only include the stimulus response and offset periods (seconds 4-12 of each 12-sec trial). Truncated mean response timecourses for the four stimulus directions were then concatenated for each sensory condition. We then found the correlation coefficient between these direction-concatenated mean PSTHs for multi-sensory trials (airflow + stripe) versus airflow only or stripe only.

Response-by column analyses included additional metrics. To calculate the mean orientation tuning of each neuron, we first converted the mean spiking response to each airflow direction into a vector, with an angle corresponding to the airflow direction and a magnitude equal to the mean response to that direction. We then calculated the mean vector across the response vectors corresponding to the 8 stimulus directions that we used. The angle of this mean vector is plotted in Fig. 4E.

Airflow response dynamics were examined using the response to ipsilateral airflow. We computed the cumulative sum to the PSTH during the full 4-sec stimulus period, and divided this timecourse by the integral of the PSTH over the entire 4 seconds (Fig. 4J). We additionally found the time when each cell's cumulative normalized response reached 0.5, or half its total response (Fig. 4K).

Analysis of Behavioral Data

Flight simulator data was collected at 50 Hz as the difference in wingbeat angles (ΔWBA, raw behavior — see Fig. 6) and integrated orientation (cumulative sum of the feedback signal to the

arena motor, see above). We parsed the integrated orientation data in three ways. First, we converted the data points into vectors with an angle equal to the fly's virtual orientation on that sample, and a length of 1. The mean orientation vector was then calculated for each fly. Second, we used the length of a this mean orientation vector to evaluate orientation stability. Third, we found the fraction of samples in the integrated orientation distribution that fell between -45° and 45° (the "toward the airflow" arena quadrant). These measures are all plotted in Fig. 5.

To assess flies' responses to our airflow manipulations, we analyzed ΔWBA during a 6-sec period surrounding the stimulus manipulation (1 sec pre-stimulus and 5 sec post-stimulus). We found each fly's mean ΔWBA response across 10 repeats of each slip stimulus. We then found the cross-fly mean and SEM (Fig. 6F).

We additionally integrated ΔWBA over the 5 sec following each slip stimulus to calculate an angular "response" to that slip (Fig. 6E,G,H). Slip response magnitudes were placed into 20° bins and collapsed across slip direction for the purposes of plotting response distributions (Fig. 6E). To calculate the fraction of each slip for which flies corrected, we divided integrated slip response on each trial by the negative magnitude of the stimulus slip, then took the mean correction fraction across all trials of a given slip magnitude (long or short, see Fig. 6G). Finally, we assessed integrated slip responses as a function of airflow direction at slip onset (Fig. 6H). Mean responses were calculated by grouping this data into 45° initial airflow direction bins.

To assess flies' responses to airflow offset, we modified the sign of the raw ΔWBA signal. Because airflow generally drives "with the flow" orienting in rigidly tethered flies (Currier and Nagel, 2018), we wanted a direction-invariant measure of with-/away from airflow turning. Accordingly, we altered the sign of ΔWBA on each sample such that turns toward the airflow source were positive, and turns away from the airflow source were negative (normally, positive ΔWBA indicates rightward turns, and leftward for negative ΔWBA). We then calculated cross-fly mean airflow offset responses (Fig. 6B) as described above for the slip stimuli. For long airflow offsets, we additionally integrated ΔWBA over the 2 sec stimulus period (Fig. 6C).

Statistical Analysis

All statistical analyses used non-parametric tests corrected for multiple comparisons (Bonferroni method). For single fly data, paired comparisons were made using the Wilcoxon Sign-Rank test (MATLAB function signrank), and unpaired comparisons using the Mann-Whitney U test (MATLAB function ranksum). Cross-fly (per-genotype) distributions were compared using the Kolmogorov-Smirnov test (MATLAB function kstest2). Significance values for all tests are reported in the Figure Legends.

Connectomic Analysis

Data from the fly hemibrain connectome (Xu et al., 2020) was visualized using neuPRINT explorer (*neuprint.janelia.org*). We identified P-F_2N_3 as PFNa in this dataset on the basis of NO

innervation and nomeclature of Wolff et al., 2015. Similarly, P-F_1N_3 was identified as PFNm and PFNp. Based on the connectivity data for an example LNa neuron (1508956088), we determined that P-F_2N_3 neurons comprise roughly 95% of the synaptic inputs onto LNas, which receive input in the NO and send output to the LAL. P-F_1N_3 neurons accounted for nearly 100% of inputs onto an example LCNpm neuron (1513363614), which similarly receives NO input and gives LAL output. Each example cell received input from all CX columns.

DNa02 is known to receive input in the LAL and drive ipsilateral turning (Rayshubskiy et al., 2020). This neuron (1140245595) is not known to receive direct input from LNa or LCNpm, but almost 30% of DNa02 inputs in the LAL are not yet accounted for. Thus, the connection proposed in Fig. 7 is based primarily on anatomical overlap. Additionally, DNa02 is known receive direct input from P-F_3LC neurons, which were also recorded as part of this study.

DATA AND SOFTWARE AVAILABILITY

All electrophysiology, behavior, and anatomy data will be made publicly available on Dryad on publication. Code for analysis will be made available on Github on publication.

KEY RESOURCES TABLE

REAGENT or RESOURCE	SOURCE	IDENTIFIER
Antibodies		
mouse anti-NC82	Developmental Studies Hybridoma Bank	RRID: AB_2314866
chicken anti-GFP	Thermo Fisher Scientific	PA1-9533
streptavidin Alexa Fluor 568	Thermo Fisher Scientific	S-11226
anti-mouse Alexa Fluor 633	Thermo Fisher Scientific	A-21052
anti-chicken Alexa Fluor 488	Thermo Fisher Scientific	A-11039
Experimental Models: Organisms/Strains		
SS52244-GAL4	Bloomington Drosophila Stock Center	RRID: BDSC_86596
SS02255-GAL4	Bloomington Drosophila Stock Center	RRID: BDSC_75923
SS00078-GAL4	Bloomington Drosophila Stock Center	RRID: BDSC_75854
SS52577-GAL4	Bloomington Drosophila Stock Center	RRID: BDSC_86625
SS54295-GAL4	Bloomington Drosophila Stock Center	RRID: BDSC_86624
SS02239-GAL4	Bloomington Drosophila Stock Center	RRID: BDSC_75926
SS54549-GAL4	Bloomington Drosophila Stock Center	RRID: BDSC_86603
R12D09-GAL4	Bloomington Drosophila Stock Center	RRID: BDSC_48503
R44B10-GAL4	Bloomington Drosophila Stock Center	RRID: BDSC_50202
(empty)-GAL4	Bloomington Drosophila Stock Center	RRID: BDSC_68384
10xUAS-IVS-syn21-GFP-p10 (attP2)	Michael Dickinson	N/A
13xUAS-Kir2.1-eGFP/TM3	Michael Reiser	N/A